

Water Resources Research®

RESEARCH ARTICLE

10.1029/2024WR037407

Key Points:

- Catchment scale groundwater modeling highlights base flow characteristics of river networks
- River base flow bears the signature of aquifer recharge, catchment morphology, and hydrogeological properties
- Changes in groundwater recharge modify the portion of the river network that receives the contribution of groundwater

Supporting Information:

Supporting Information may be found in the online version of this article.

Correspondence to:

A. Bellin,
alberto.bellin@unitn.it

Citation:

Betterle, A., & Bellin, A. (2024). Morphological and hydrogeological controls of groundwater flows and water age distribution in mountain aquifers and streams. *Water Resources Research*, 60, e2024WR037407. <https://doi.org/10.1029/2024WR037407>

Received 1 MAR 2024

Accepted 21 SEP 2024

© 2024. The Author(s).

This is an open access article under the terms of the [Creative Commons Attribution-NonCommercial-NoDerivs License](#), which permits use and distribution in any medium, provided the original work is properly cited, the use is non-commercial and no modifications or adaptations are made.

Morphological and Hydrogeological Controls of Groundwater Flows and Water Age Distribution in Mountain Aquifers and Streams

A. Betterle^{1,2}  and A. Bellin² 

¹Joint Research Centre, European Commission, Ispra, Italy, ²Department of Civil, Environmental and Mechanical Engineering, University of Trento, Trento, Italy

Abstract Mountains are an essential source of the terrestrial component of the hydrological cycle, supplying high-quality water to river networks and floodplain aquifers, especially during droughts. Traditionally, mountain hydrology has focused on shallow processes, overlooking the significance of deep-seated rock formations due to characterization challenges. Recent field studies have revealed that fractured rock formations can host rich aquifers despite their low permeability. Nonetheless, it is unclear how deep flows interact with the overall hydrological functioning of mountain areas, how they contribute to the long-term water budget, and how climate, morphology, and geology jointly control them. Through numerical simulations, we have gained new insights into mountain aquifers, addressing (a) the proportion of groundwater base flow and its age distribution, (b) water storage and its sensitivity to groundwater recharge, (c) the impact of long term mean recharge on the extent of the groundwater-fed surface drainage network under various morphological and geological settings. We showed that subsurface travel times follow a Gamma distribution, whose parameters are modulated by recharge, hydraulic conductivity, and topography. High recharge and strong decay with depth of the hydraulic conductivity in a hilly topography lead to a shallow water table mimicking the surface topography and spatially distributed low-intensity outflows that feed a dense drainage network. In rugged catchments, the groundwater contribution intensifies and concentrates in the downstream portion of the river network as recharge declines. These findings can help assess how a changing climate might impact hydrological regimes under various geomorphological conditions and identify sustainable water uses in mountain environments.

Plain Language Summary Mountainous regions cover a large portion of the planet. These areas are at the origin of the terrestrial component of the water cycle, supplying high-quality water to river networks and downstream floodplains where most of the human population dwells. Mountains feed the hydrological cycle with a large amount of water compared to surrounding floodplains, and their large storage capacity is crucial for mitigating climatic variability and sustaining downstream habitats, particularly during droughts. Traditionally, deep water flows in mountain formations have been overlooked because they are considered less important than near-surface flows. However, recent surveys have revealed that fractured rock formations can host a significant amount of flowing water, raising questions about the contribution of these flows to long-term water budgets and their susceptibility to environmental factors. With this in mind, we investigate the impact of climate, geology, and topography on subsurface flows and assess the vulnerability of mountain aquifers to climate change. Our findings indicate that in mountain regions, a reduction in groundwater recharge, which may be caused by climate change, leads to a decrease in the extent of the river network with permanent flow. These results provide valuable insights into the potential effects of climate change on water resources.

1. Introduction

Mountains encompass about 25% of Earth's surface across climatic, ecological, and geological gradients (Meybeck et al., 2001). They receive disproportionate precipitation, providing abundant and high-quality water to nearly 40% of the world's population (Immerzeel et al., 2020; Markovich et al., 2019; Viviroli et al., 2020). Additionally, they are a major source of energy through hydro-power, which in 2021 satisfied 17% of the global energy demand (IEA, 2021).

Water storage in mountain areas has traditionally been associated with solid water in snow caps and glaciers, liquid surface waters in lakes and reservoirs, or in high-yield aquifers hosted in basin-fill loose sediments along valley bottoms (Huss et al., 2017; Käser & Hunkeler, 2016). Only recently, the importance of groundwater

storage in mountain massifs has been recognized for sustaining water resources and mitigating the impact of droughts (Hahm et al., 2022; Wolf et al., 2023). Consequently, in the last decade, groundwater has been introduced into large-scale hydrological and Earth Systems Models (ESMs) (de Graaf et al., 2015; Maxwell et al., 2015; Müller Schmied et al., 2021; Naz et al., 2023; Reinecke et al., 2019), after acknowledging that, without this component, future hydrological projections would be biased (Clark et al., 2015). However, many challenges remain in the parametrization of aquifers, including the often overarching difficulties in the characterization of hydrogeological properties, which is one of the significant sources of uncertainty affecting simulation results (Yang et al., 2023).

Efforts have been made to implement subsurface flow into catchment-scale hydrological models (Camporese et al., 2010). However, despite the widely recognized importance of groundwater in shaping base flow, most studies deal with short-term shallow hillslope contribution (Benettin et al., 2022; Jencso et al., 2009; Tromp-van Meerveld & McDonnell, 2006). This focus on shallow flows is probably sprouting from the rapid streamflow dynamics that characterize mountain streams (Abe et al., 2020). Indeed, relatively thin soils and hydraulically conductive loose deposits overlaying weathered rocks in steep environments have been thought to promote fast streamflow responses to rainfall events (Benettin et al., 2022; Fiori & Russo, 2007, 2008; Hayashi, 2020; Welch & Allen, 2014). The underlying assumption of this conceptual model is that the contrast in hydraulic conductivity between the surface soil layer and the rock underneath makes deep circulation a minor streamflow component.

The necessity of changing this “shallow view” by introducing lateral ridge-to-valley shallow and deep flows into ESMs has been evidenced in the review by Fan et al. (2019), and Condon et al. (2020) discussed the importance of including deep flows into hydrological modeling of mountain areas. Several studies have shown that aquifers develop in most mountain areas, even in poorly permeable formations, as a substantial fraction of precipitation infiltrates into the fractured bedrock (Abe et al., 2020; Grant & Dietrich, 2017; Hahm et al., 2022; Maréchal & Etcheverry, 2003; Tiedeman et al., 1998; Winter et al., 2003). Groundwater developing in poorly permeable rock formations is prone to “geologically” extended residence times. However, the tendency of activating extremely long residence times is mitigated by the high topographic gradients, thereby enhancing the importance of mountain aquifers as a vital component of the hydrological cycle (Fan et al., 2019; Wörman et al., 2007). These aquifers feed springs and are fundamental to sustaining river base flow during recession periods, particularly in dry climates or during droughts (Katsura et al., 2009; Rempe & Dietrich, 2018).

Due to their relatively low permeability, rock formations in mountain areas can store large volumes of water for extended periods and release them with reduced temporal variability, as compared to the intermittent nature of rainfall (Di Dato et al., 2023; Forster & Smith, 1988a, 1988b; Hayashi, 2020). Consequently, mountain aquifers buffer extreme hydrological events and increase the resilience of water bodies to climate change (Immerzeel et al., 2010, 2020). Additionally, groundwater plays a vital role in regulating the biochemical cycles of the Earth's critical zone through processes such as rock weathering and chemical dissolution (Benettin et al., 2022; Katsura et al., 2009; Queloz, Bertuzzo, et al., 2015; Queloz, Carraro, et al., 2015; Rempe & Dietrich, 2018; Rinaldo et al., 2020; Rodriguez-Iturbe et al., 2009). From the ecological point of view, it mediates between the terrestrial and fluvial compartments of the Earth's ecosystems (Battin et al., 2023).

Despite its importance, the hydrological behavior of mountain aquifers is poorly known. This lack of knowledge, which limits our capability to manage and protect this vital water resource, is the consequence of often overwhelming difficulties in characterizing fundamental hydrogeological properties, such as the spatial distribution of hydrofacies and their permeability, and scarce hydraulic head measurements (Hayashi, 2020). In an attempt to overcome these limitations, a few studies analyzed the sensitivity of water flows to hydrological forcing and geomorphological traits of the landscape (Gleeson & Manning, 2008; Katsura et al., 2009; Rapp et al., 2020). Alternatively, in a synthesis effort, other studies have suggested framing groundwater flow as a self-organized process controlled by fundamental thermodynamic principles (Berkowitz & Zehe, 2020; Schiavo, 2023; Zehe et al., 2021). Because of the challenges in characterizing the subsurface and the complex interactions and feedbacks with surface waters, the effects of hydrogeological/morphological settings on the age of groundwater and streamflow have seldom been investigated, despite water age being widely recognized as a driver of water quality (Benettin et al., 2022). Furthermore, the hydrology of mountain areas has been explored so far with a surface hydrology perspective, focusing on relatively fast runoff responses at the hillslope scale. At the same time, deeper and longer pathways are neglected or treated in a simplified manner (Kollet & Maxwell, 2008; Leray et al., 2016). On the other hand, the hydrogeological perspective taken by

other studies neglects short, superficial flow pathways, regardless of their importance for the rapid hydrological dynamics and streamwater quality (Staudinger et al., 2019).

Environmental and artificial tracers have been employed in the field to explore subsurface flows (Gonfiantini et al., 1998; Hrachowitz et al., 2010; McGuire et al., 2005), as well as to assess groundwater contribution to streamflow (Klaus & McDonnell, 2013; Paul Köeniger & Stichler, 2009; Penna et al., 2016, 2017). While using tracers has proven enlightening, it is time-consuming and poses technical challenges that demand specific expertise. For instance, direct inference of flowpath lengths from tracer and stable isotopes is unattainable, and accurate interpretation of the data requires a comprehensive understanding of environmental processes influencing tracer stability and isotopic fractionation (Klaus & McDonnell, 2013; McGuire et al., 2005). Therefore, simultaneous consideration of multiple tracers is essential for adequately sampling the typically broad range of residence times of subsurface flows. Unfortunately, the most common tracers in hydrology are insensitive to residence times larger than a few years, thereby obscuring the effects of deep and slow flowpaths (Rodriguez et al., 2021; Seeger & Weiler, 2014; Stewart et al., 2021). At the same time, the investigation of longer residence times offered by tracers such as tritium is often hampered by short records (Stewart et al., 2021). Ideally, to elucidate the entire spectrum of travel times, tracer data resolving both short and long residence times should be collected simultaneously and interpreted with models able to capture the corresponding flowpaths (Benettin et al., 2017; Seeger & Weiler, 2014; Stadnyk & Holmes, 2023; Visser et al., 2019). In this context, spatially distributed and physically-based numerical models remain indispensable for understanding the subsurface water flows. In particular, models can bridge the gap between the timescales of specific tracers and provide a unified framework to investigate groundwater flows.

In the present study, our primary focus is on addressing the following questions: (a) What is the impact of recharge, hydrogeological properties, and surface topography on groundwater flow and the distribution of water travel times in mountainous areas? (b) How do hydrogeological and morphological characteristics at the catchment scale influence the slow and fast hydrological responses, and how is this reflected in the age of streamflow? (c) To what extent do the aforementioned geomorphoclimatic variables influence the resilience of groundwater resources to climate change and the extent of the persistently active drainage network in mountain environments?

We address these questions through simulations with a physically based and spatially distributed 3-D model of the unconfined groundwater flow system of a representative mountain catchment, and in two additional hypothetical catchments obtained by rescaling the elevations of the above catchment. The model is described in Section 2, the results are presented in Section 3, followed by their discussion in Section 4, and conclusions are drawn in Section 5.

2. Materials and Methods

A geological profile of mountain formations typically features a thin superficial organic layer of soil ($0 \div 3$ m) overlaying $0 \div 10$ m of highly weathered bedrock called saprolite (Welch & Allen, 2014). Underneath these surface layers is a $0 \div 200$ m thick unweathered fractured rocks layer, overlaying a low- K bedrock. According to this geological structure, the saturated hydraulic conductivity K decreases with depth, from about $10^{-3} \div 10^{-4}$ m/s in the superficial loose material to $10^{-6} \div 10^{-9}$ m/s in the deeper unweathered fractured bedrocks (Welch & Allen, 2014).

In the present work, and in line with other studies (Caine, 2006; Caine & Tomusiak, 2003; de Graaf et al., 2015; Gleeson & Manning, 2008; Manning et al., 2009; Maxwell et al., 2015; Welch & Allen, 2014), we simulated both the superficial loose material and the fractured bedrock below as an equivalent porous media with the hydraulic conductivity that declines with depth. Local effects of faults and large fractures are not included because our objective is to analyze the general characteristics of the groundwater flow systems. The effects of these features may be relevant in some cases but cannot be generalized, and thereby, they can only be addressed on case-specific bases.

2.1. Flow Equation

Subsurface saturated water flow is controlled by the hydraulic properties of the formation and by boundary conditions accounting for the hydro-climatic forcing and geological constraints at the domain's frontiers. The

governing Equation is obtained by coupling mass balance with Darcy's law, and under stationary conditions, it assumes the following form:

$$\frac{\partial}{\partial x_1} \left[K(\mathbf{x}) \frac{\partial h(\mathbf{x})}{\partial x_1} \right] + \frac{\partial}{\partial x_2} \left[K(\mathbf{x}) \frac{\partial h(\mathbf{x})}{\partial x_2} \right] + \frac{\partial}{\partial x_3} \left[K(\mathbf{x}) \frac{\partial h(\mathbf{x})}{\partial x_3} \right] + r(\mathbf{x}) \delta[x_3 - \eta(x_1, x_2)] = 0 \quad (1)$$

where $\mathbf{x} = (x_1, x_2, x_3)$ are the spatial coordinates, h [L] is the hydraulic head, K [$L T^{-1}$] is the spatially variable, yet isotropic, hydraulic conductivity and r [$L T^{-1}$] is the recharge. In addition, $\delta[\cdot]$ [L^{-1}] is the Dirac Delta distribution and η [L] is the elevation of the water table.

The specific water discharge $\mathbf{q} = (q_1, q_2, q_3)$ [$L T^{-1}$] obeys to the Darcy's equation:

$$q_i(\mathbf{x}) = -K(\mathbf{x}) \frac{\partial h(\mathbf{x})}{\partial x_i}, \quad i = 1, 2, 3 \quad (2)$$

In line with the general hydraulic characteristics of mountain aquifers described above, we assume that the hydraulic conductivity decreases exponentially with depth (Wörman et al., 2007):

$$K(\mathbf{x}) = K_G e^{-\alpha[z(x_1, x_2) - x_3]} = K_G k(\mathbf{x}) \quad (3)$$

where $z(x_1, x_2)$ is the ground surface elevation, K_G is the hydraulic conductivity at the ground surface, $k(\mathbf{x}) = \exp\{-\alpha[z(x_1, x_2) - x_3]\}$ is a dimensionless function controlling the decay of the hydraulic conductivity with depth, and α [L^{-1}] is the decay rate. After replacing Equation 3 into Equation 1 the flow equation becomes:

$$\frac{\partial}{\partial x_1} \left[k(\mathbf{x}) \frac{\partial h(\mathbf{x})}{\partial x_1} \right] + \frac{\partial}{\partial x_2} \left[k(\mathbf{x}) \frac{\partial h(\mathbf{x})}{\partial x_2} \right] + \frac{\partial}{\partial x_3} \left[k(\mathbf{x}) \frac{\partial h(\mathbf{x})}{\partial x_3} \right] + R(\mathbf{x}) \delta[x_3 - \eta(x_1, x_2)] = 0 \quad (4)$$

where $R = r/K_G$ [–] is the dimensionless recharge.

The flux \mathbf{q} is controlled by: (a) the geometric constraints of surface topography, leading to the formation of seepage faces at the ground surface; (b) the ratio $R = r/K_G$ with r representing the climatic forcing and K_G epitomizing the hydrogeologic properties of the geological formation; (c) the heterogeneity of the hydraulic conductivity represented here through the decay function $k(\mathbf{x})$, according to the model (Equation 3). Figure 1b shows the vertical distribution of the hydraulic conductivity along two representative north-south and west-east catchment sections for $\alpha = 0.001 \text{ m}^{-1}$. The distributions for a lower and a higher decay rate are shown in the Supplementary Information. The figure shows that the adopted model of spatial variability mimics the typical layering observed in mountain formations.

2.2. Modeling Approach

The present work analyzes the groundwater flow field that develops in the formations described in Section 2.2.1 under the effect of the long-term mean potential recharge r_{pot} [$L T^{-1}$], which is the maximum possible aquifer mean recharge controlled by the dominant climate and vegetation, with $R_{pot} = r_{pot}/K_G$, being its dimensionless counterpart. However, the actual aquifer recharge r may be lower where the water table rises to the surface. The simulations seek to identify the prevailing long-term (dynamic) equilibrium conditions of mountain aquifers. Non-equilibrium conditions, such as the onset and development of a drought, when the recharge is persistently smaller than the groundwater contribution to base flow—or the recovery from droughts when recharge is larger than base flow—are not explicitly considered. Instead, we focus on the long-term prevailing equilibrium condition, when groundwater contribution to base flow is balanced by recharge. We also investigate the interplay between climate and geomorphology on the long-term average base flow. However, under the hypotheses of a slow varying recharge, the simulations provide evidence of base flow changes due, for instance, to climate change. In fact, slow groundwater dynamics forced, for example, by long-term alterations of the recharge, can be interpreted as a sequence of steady states.

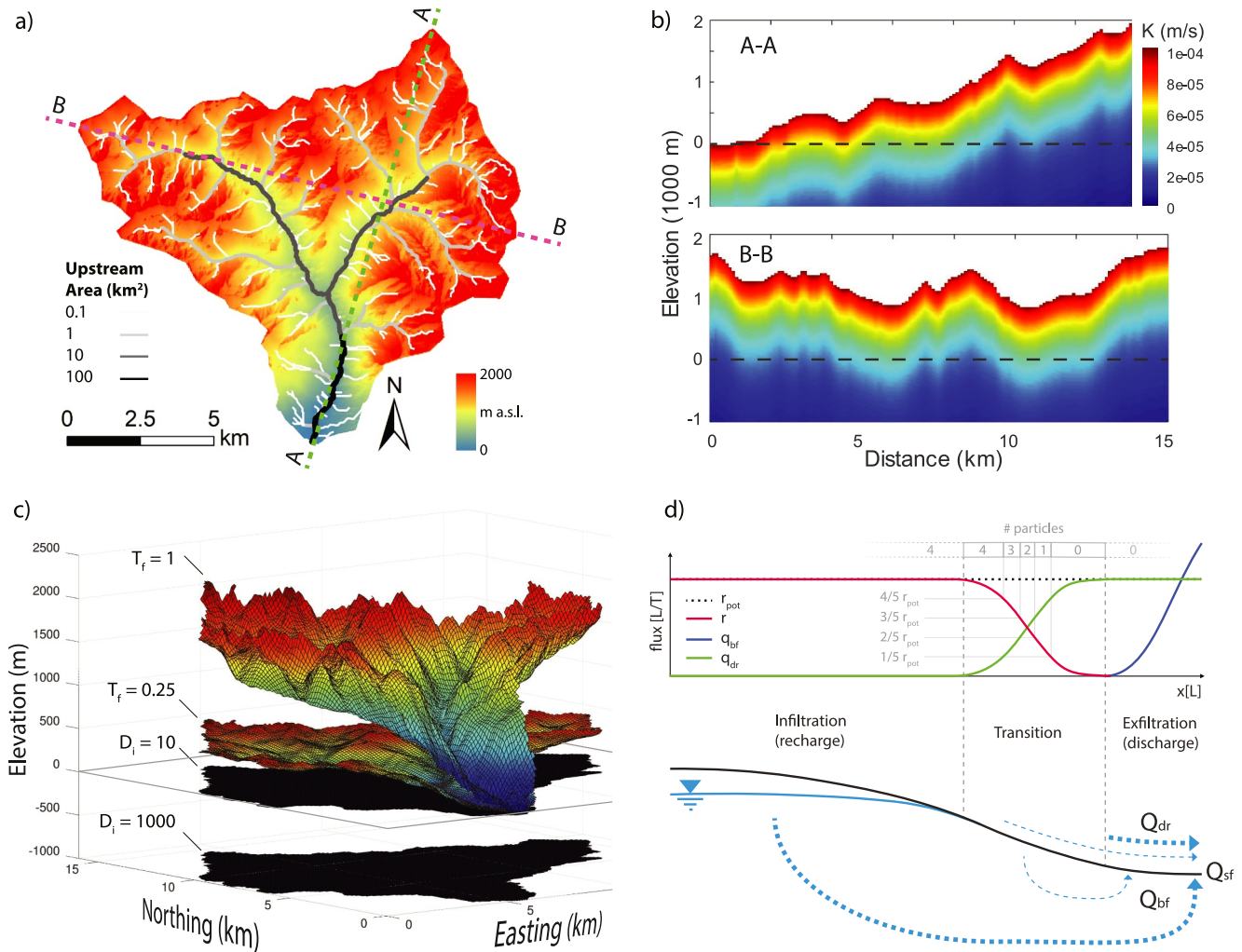


Figure 1. (a) Topography of the reference catchment, with the surface drainage network for a set of threshold contributing areas identified by changing colors and line thicknesses; (b) Hydraulic conductivity profiles along the cross-sections A-A and B-B (see panel a) for $T_f = 1$, $D_i = 1000$ m and $\alpha = 0.001$ m⁻¹ (more examples are shown in Supporting Information S1); (c) Representation of two out of three reliefs considered in this study: the reference catchment ($T_f = 1$) and a smoothed hilly relief version obtained from Equation 5 with $T_f = 0.25$. The horizontal surfaces represent two out of the three bottom impervious boundaries of the domain, located at a depth from the catchment outlet of $D_i = 10$ m and $D_i = 1000$ m, respectively; (d) sketch of the hydrological fluxes of interest: the local partitioning of the incoming potential recharge r_{pot} (into actual groundwater recharge r and direct runoff Q_{dr}), and upwelling groundwater Q_{bf} . Notice that Q_{dr} and Q_{bf} are the sum of the local contributions across the cells where the water table reaches the ground surface (i.e., $Q_{dr} = \sum q_{dr} A_c$ and $Q_{bf} = \sum q_{bf} A_c$, with A_c being the horizontal area of the cell), and represent the fast (young) and slow (old) component of the streamflow Q_{sf} , respectively. The number of particles injected in recharge areas to compute flowpath lengths and residence times is proportional to the ratio between the actual local recharge r and the potential recharge r_{pot} (see Section 2.3).

The present study is based on conceptualizing the groundwater flow system as an unconfined mountain aquifer under steady-state conditions described by Equation 4 and with suitable boundary conditions. The simulations were performed with MODFLOW-NWT, a Newton-Raphson formulation of MODFLOW-2005 that is particularly suited for solving unconfined groundwater flow systems characterized by steep gradients and for tackling situations where drying and rewetting nonlinearities challenge the traditional MODFLOW solver (Niswonger et al., 2011). The code solves for the hydraulic head h in a regular three-dimensional grid under suitable boundary conditions. As output, MODFLOW-NWT provides the distribution of the hydraulic head and the flow field. In this study, all the models were built in Python via FloPy (Leaf & Fienen, 2022): a library specifically designed to perform MODFLOW simulations (Bakker et al., 2024).

The models are designed to capture water outflows where the water table naturally emerges at the seepage faces. Outflow areas result from the solution of the flow equation in the computational domain delimited by the surface

topography of the catchment and by impervious surfaces enclosing the flow domain: horizontally (at the bottom); and vertically (along the morphological divides of the catchment). The impervious vertical boundary is equivalent to assuming that the subsurface water divide coincides with the watershed water divide. The assumption is consistent with the hypothesis of hydraulic conductivity varying along the vertical direction only and has been widely adopted starting from the pioneering work of Tóth (1962, 1963). In the absence of specific information, the same no-flow condition is assigned to the catchment outlet. Consequently, subsurface regional flows are neglected, and the within-catchment long-term return flow equals the long-term mean recharge. In this conceptualization the recharge is the infiltration below the root zone, which becomes available for groundwater flow in the saturated zone. The unsaturated zone is not modeled, and recharge is applied to the water table.

The modeling approximations reflect the potential of the catchment to develop seepage faces and humid areas. Note that the assumptions may not represent well contexts where intense dynamics affect the vertical fluxes in the unsaturated zone. Furthermore, the location of perennial springs may depend on the local distribution of faults and fractures and/or on heterogeneity of the hydraulic conductivity not explicitly considered in the heterogeneity model (Equation 3). Although neglecting such features is an approximation, they are site-specific, and their effects on base flow can hardly be generalized.

2.2.1. Computational Domain

The Maso catchment with the control section at Borgo Valsugana, Italy (46.073°N, 11.497°E) serves as a morphological reference for the analysis. The total contributing surface area A at the control section is of 125 km², and elevation ranges between 400 and 2600 m a.s.l., with a mean of 1700 m a.s.l. and a standard deviation of 400 m. The fifth order-river network shown in Figure 1a is extracted using a 30 m Digital Terrain Model of the catchment with a threshold drainage area of 0.1 km² (Hawker et al., 2022).

The elevation $z_0(\mathbf{x})$ of the reference catchment is translated and rescaled as:

$$z(\mathbf{x}) = T_f(z_0(\mathbf{x}) - z_{0,\min}) \quad (5)$$

where T_f is a topography factor and $z_{0,\min}$ is the minimum catchment elevation (i.e., the elevation of the catchment's outlet). Hence, $T_f > 1$ generates a topography rougher than the reference one, while a smoother topography is obtained with $T_f < 1$, as shown in Figure 1c. Furthermore, the computational domain is extended to a depth D_i [L] below the control section at the catchment's outlet, which is at zero elevation. With this conceptual model, the two parameters, T_f and D_i , are used to quantify the effects of the topography and the depth of the impervious basal rock formation, respectively. In the present work, we considered the two extreme depths of $D_i = 10$ m and $D_i = 1000$ m, with the latter exceeding the depth of active groundwater circulation indicated of the order of hundred meters (Gleeson & Manning, 2008; Manning & Caine, 2007; Markovich et al., 2019). The objective here is to explore the importance of deep flowpaths along the lines suggested in the commentary by Condon et al. (2020). Notice that this conceptual model cannot be applied to evaluate the contribution of the mountain aquifer to an adjacent floodplain aquifer or conterminous catchments due to the assumption of impervious lateral boundaries, as discussed in Section 2.2.2. Assessing this component of the hydrological cycle, whose importance has been brought up in a review paper by Fan et al. (2019), is beyond the objective of the present work. Finally, the same porosity n is assumed for the soil and the underlying rock formation.

2.2.2. Hydroclimatic Forcing and Boundary Conditions

Locally, the water table may intersect the ground surface, causing seepage. Drainage across seepage faces is simulated using the Drain (DRN) package of MODFLOW (Harbaugh, 2005). The package simulates drainage by removing water from a cell when the local head is higher than the prescribed elevation of the drain, which we set coincident with the catchment's surface. All surface cells are defined as drains, and the local seepage discharge, $Q_{bf,i}$ [L³ T⁻¹] for the i -th surface cell is computed as follows (Harbaugh, 2005):

$$Q_{bf,i}(\mathbf{x}) = \begin{cases} CD [h(\mathbf{x}) - z(\mathbf{x})], & \text{for } h(\mathbf{x}) > z(\mathbf{x}) \\ 0, & \text{otherwise} \end{cases} \quad (6)$$

Table 1
Parameters Used in the Model Runs

Parameter	Description	Values	Units
R_{pot}	Dimensionless potential recharge	0.001, 0.002, 0.005, 0.01, 0.02, 0.05, 0.1, 0.2, 0.5, 0.65, 0.8, 1	–
α	Decay rate of hydraulic conductivity	10^{-4} , 10^{-3} , 10^{-2}	m^{-1}
T_f	Topographic stretch factor	0.25, 1, 4	–
D_i	Depth of the flow domain	10, 100, 1000	m

Note. All possible combinations of parameters are explored in the simulations.

where $CD [L^2 T^{-1}]$ is the drain conductance. To ensure that $h = z$ at the seepage cells and remove the water exceeding saturation, CD is set to 10^4 times the cell's conductance. Consequently, the total base flow Q_{bf} can be computed as:

$$Q_{bf} = \sum_{i=1}^{N_s} Q_{bf,i} \quad (7)$$

with the summation extended to all the N_s saturated surface cells where $h > z$.

The recharge is assigned at the water table (in the uppermost active, i.e. saturated, cells of the computational domain) using the MODFLOW RCH package (Harbaugh, 2005). At the seepage cells, the recharge is set to zero and the flow rate $r_{pot} A_c$, where A_c is the cell's horizontal area, is assigned to the fast direct runoff Q_{dr} . When $h(\mathbf{x}) < z(\mathbf{x})$, but higher than the bottom of the surface cell, only the fraction of $r_{pot} A_c$ that saturates the cell is applied, and the remaining is assigned to the direct runoff. Thus, actual recharge r is in the range $[0, r_{pot}]$ depending on the local interaction between the ground surface elevation and the underlying water table level, and it is greater than zero only where groundwater outflow is absent (see Figure 1d). As depicted in Figure 1d and in line with Forster and Smith (1988a), three conditions may occur when the water table interacts with surface topography: (a) $r = r_{pot}$ and $q_{dr} = q_{bf} = 0$ where the water table lays below the ground surface; (b) $r = 0$ and $q_{dr} = r_{pot}$ where groundwater exfiltrates (i.e., where groundwater flows across the ground surface as base flow q_{bf}); (c) $q_{dr} = r_{pot} - r$ and $q_{bf} = 0$ where the recharge needed to saturate the surface cell is smaller than the potential recharge. Here, q indicates the flow per unit surface across the horizontal cell's surface. Hence, the water table at the ground surface is a necessary, though not sufficient, condition to generate seepage, as some net input of water may still be needed to maintain the water table at the ground surface. On the other hand, no recharge occurs at seepage faces with groundwater outflow given by Equation 6. Similarly to Equation 7, the spatial integral of q_{dr} across the catchment is assumed to constitute the quick runoff component of the streamflow (Q_{dr}).

2.2.3. Numerical Discretization and Model Runs

The computational domain is discretized into 100 layers featuring squared cells with 100 m horizontal sides. The thickness of the layers scales as a function of the vertical extent of the domain: from about 100 m when $T_f = 4$ and $D_i = 1000$ m, to 6 m when $T_f = 0.25$ and $D_i = 10$ m (see Section 2.2.1). The number of saturated (active) cells varies depending on the water table configuration from approximately 1×10^4 (when the water table is deep and flat) to 5×10^5 , (when the water table is high and mimics the ground surface).

Overall controls of the flow field are: $R_{pot} = r_{pot}/K_G$, α , T_f , and D_i . Table 1 shows the range of variation of these parameters explored in the simulations. Specifically, R_{pot} ranges from dry conditions and/or permeable formations to wet conditions and/or poorly permeable formations. Hydraulic conductivity is fairly homogeneous with depth for $\alpha = 10^{-4} m^{-1}$ ($K(d) = K_G/2$ for $d \simeq 7000$ m) whereas it decreases sharply for $\alpha = 10^{-2} m^{-1}$ ($K(d) = K_G/2$ for $d \simeq 70$ m). From the morphological point of view, $T_f = 0.25$ smooths the reference relief ($T_f = 1$), producing a hilly landscape with differences in elevations of a few hundred meters, whereas $T_f = 4$ stretches the elevation approaching the rougher reliefs observed on Earth (e.g., a Himalaya type relief). Finally, deep circulation is limited when a small D_i is considered.

The examined scenarios include all possible combinations of the previous parameters, totaling 324 models. Simulations are performed on a dual 6-core CPU machine (Intel Xeon C5-2620 v2) with 44 GB of RAM. The total processing time is 1.5 days, with 10 runs performed in parallel.

2.3. Particle Tracking and Travel Times

The travel time of a water parcel (particle) is a widely used concept in groundwater (Cvetkovic & Dagan, 1994; Cvetkovic et al., 2012; Dagan, 1989; Rubin, 2003) and in catchment hydrology (Botter et al., 2005, 2011). Travel time is defined as the time the particle spends inside the catchment, or alternatively, as its age when it exits from one of the possible outlets (the age of a particle is the difference between the actual time and the time the particle entered the system). Under time-varying flow fields, particles entering the domain at the same position but at different times show different travel times (and flowpaths). At the same time, they share the same travel time (and flowpaths) under steady-state conditions (Botter et al., 2011; Niemi, 1977), as commonly assumed in hydrogeology (Dagan, 1989; Rubin, 2003). Given the steady-state flow assumption, the latter case is that of the present work. Travel times can be computed by tracking water parcels from their entry points at the water table to the points where they exit the computational domain.

Particle tracking is performed by the software MODPATH (Pollock, 2016). The number N of particles released within a given cell intersected by the water table is computed as: $N = \lceil \frac{r}{r_{pot}} N_p \rceil$, where the function $\lceil \cdot \rceil$ is the closest integer larger than the argument. In doing that, N is proportional to the local recharge r . We used a maximum of $N_p = 4$ regularly distributed particles for each cell (see Figure 1d). When flow is at steady state, the flux is conserved along the streamline, and therefore, the distribution of the water age across the entire groundwater outlet coincides with the distribution of the particle travel times.

The entry flux per unit cross-section at a given streamline is $r \in [0, r_{pot}]$, depending on the local flow conditions (see Section 2.2.2). Consequently, the flux that cannot enter the streamline (i.e., $q_{dr} = r_{pot} - r$) is transferred to the outlet of the catchment with zero age, under the assumption that the time a particle spends in the surface network is negligible with respect to the subsurface travel time and that it cannot re-infiltrate.

In the following, particle travel times and ages are considered in their dimensionless form T obtained via normalization with respect to the characteristic Lagrangian time $n l / K_G$ (where $l = \sqrt{A}$ is the characteristic spatial scale, and n is the porosity). Similarly, L denotes the dimensionless flowpath length with respect to the characteristic spatial scale.

3. Results

We start by analyzing how the controlling factors, identified in the potential recharge $R_{pot} = r_{pot} / K_G$, the depth-decay rate of the hydraulic conductivity α , the topography factor T_f , and the formation's depth D_i , influence the dimensionless travel time T .

Figure 2a shows the median and the interquartile range of T as a function of R_{pot} for three values of both α (columns) and T_f (rows). Each panel shows T for both shallow ($D_i = 10$ m, blue line) and deep ($D_i = 1000$ m, red line) geological formations. As R_{pot} increases, T decreases for all the considered combinations of T_f , α and D_i . In particular, T decreases by two to three orders of magnitude, ranging from values between 1 and 10 to approximately 0.01, as R_{pot} increases by three orders of magnitude from 10^{-3} to 1. For a given R_{pot} , the travel time is larger for $D_i = 1000$ m than for $D_i = 10$ m, but their difference, which is of about one order of magnitude for small recharge, decreases as R_{pot} and T_f increase. The formation depth is, therefore, more relevant for low relief and drier climates and/or more permeable formations (i.e., small R_{pot} resulting from small r_{pot} , or large K_G).

It can be observed that R_{pot} modulates a broader range of travel times for $T_f = \{1, 4\}$ than for $T_f = 0.25$ and this effect is enhanced for large α values when the hydraulic conductivity declines rapidly with depth. On the other hand, the effect of a larger α is to reduce T in the case of low relief (i.e., for $T_f = 0.25$, first row in Figure 2), and more for $D_i = 1000$ m than for $D_i = 10$ m. Furthermore, the effect of D_i attenuates in wet climates where the main controlling factors are T_f and α . In general, T shows a power law reduction with R_{pot} in all conditions, except for the hilly topography ($T_f = 0.25$) and also for $T_f = 1$ and large α . Hence, in wet climates and/or poorly permeable

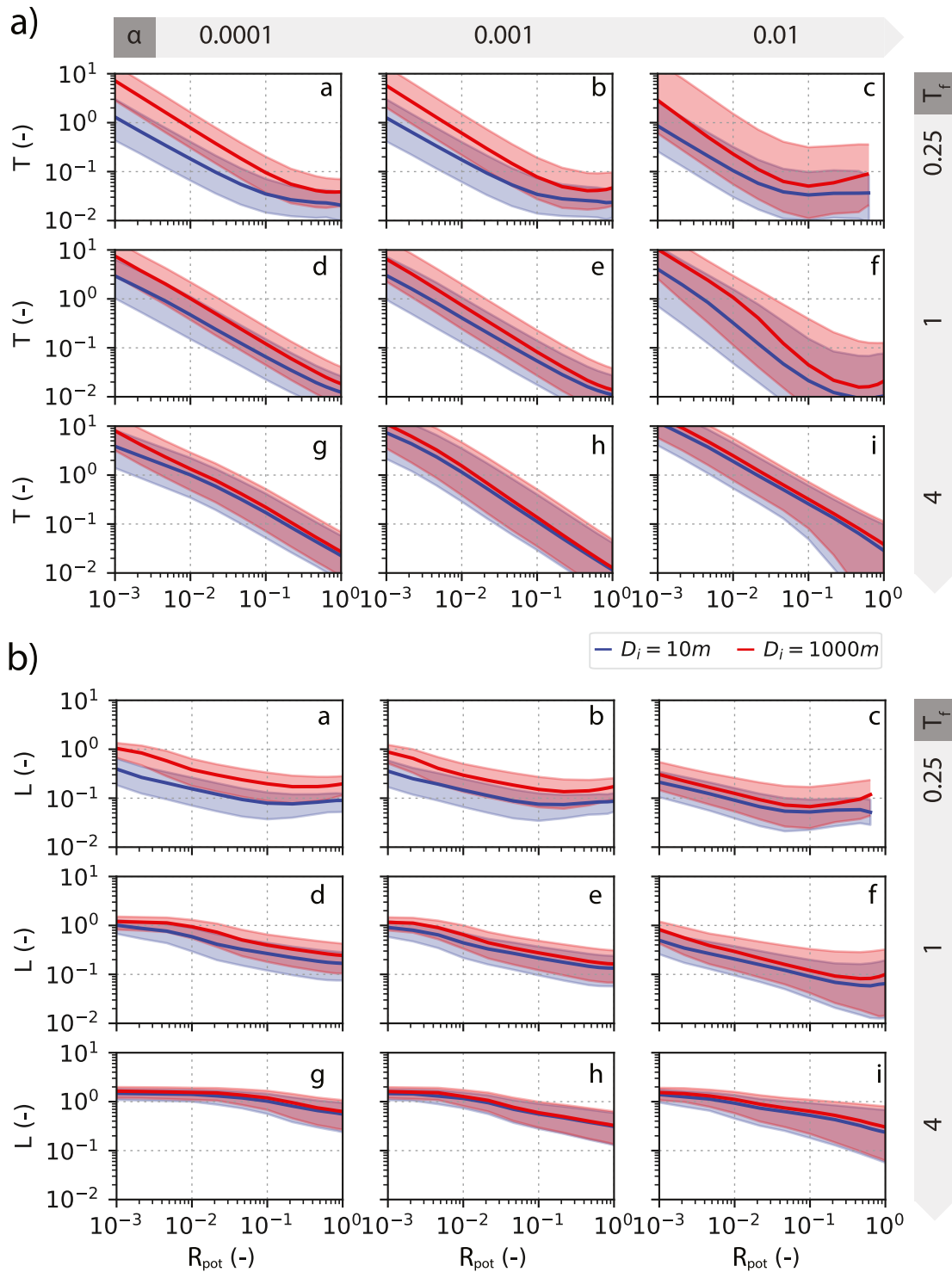


Figure 2. (a) Dimensionless travel time T as a function of the dimensionless potential recharge $R_{pot} = r_{pot}/K_G$ for three values of the hydraulic conductivity decay rate α [m^{-1}] (columns) and three topography factors T_f (rows). Solid lines indicate the median of T , and the shaded areas represent the interquartile ranges. The cases $D_i = 10\text{ m}$ and $D_i = 1000\text{ m}$ are displayed in blue and red, respectively; (b) dimensionless streamline length L under the same conditions.

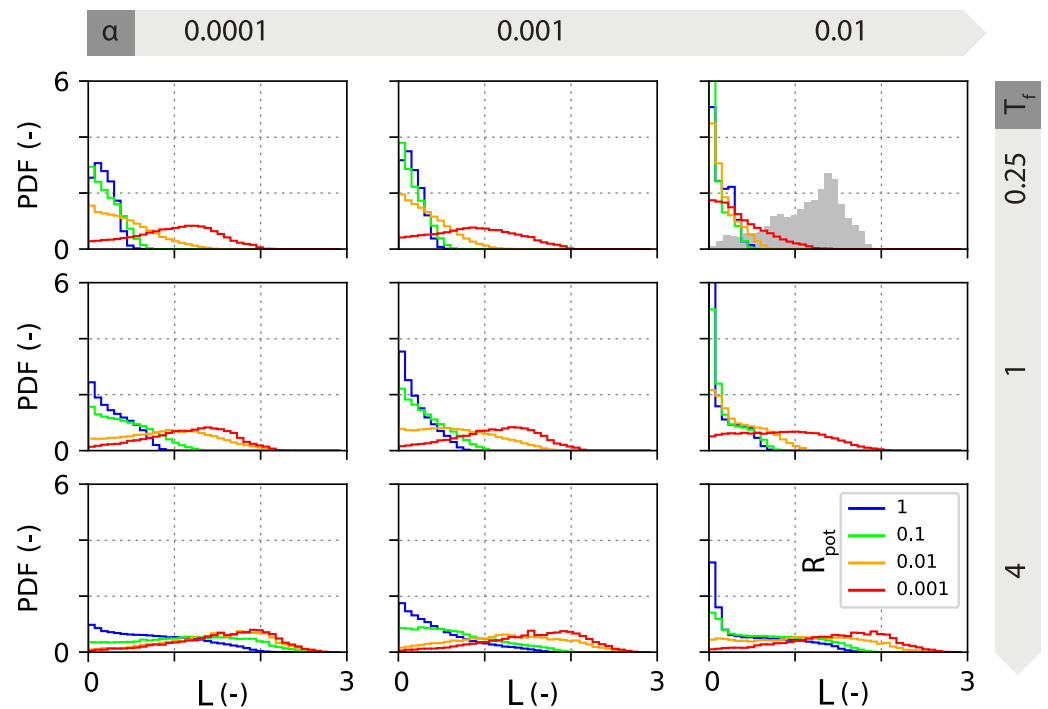


Figure 3. Probability Density Function of the dimensionless flowpath lengths for a few selected dimensionless recharge rates (R_{pot}) and different values of α [m^{-1}] and T_f . Results refer to a formation depth of $D_i = 1000$ m (see Figure S2 in Supporting Information S1 for $D_i = 10$ m). The catchment width function, which is insensitive to T_f , is shown in shaded gray on the upper-right panel.

formations, the flow field becomes topography-controlled, thereby attenuating the effect of climate, as epitomized by R_{pot} , with the $T - R_{pot}$ relationship that flattens out (Figure 2a panels c and f).

Figure 2b shows the median and the interquartile range of the dimensionless flowpath lengths L . In all cases, an increase of R_{pot} leads to shorter flowpaths. In general, the shrinkage of L as R_{pot} increases pairs with the reduction of T , but at a much smaller decreasing rate, which, in addition, is lower for higher T_f . For high relief ($T_f = 4$) and fairly homogenous hydraulic properties of the subsurface ($\alpha = 10^{-4} \text{ m}^{-1}$), the median flowpath length remains nearly constant for $R_{pot} = [10^{-3}, 10^{-1}]$ and decreases slightly for higher R_{pot} (see the panel g). As expected, D_i exerts a larger impact on L in hilly topographies ($T_f = 0.25$) than in high reliefs ($T_f = \{1, 4\}$).

The Probability Density Functions (PDFs) of the flowpath lengths and travel times highlight essential aspects of water circulation in the subsurface. Figure 3 shows that the largest effect on the PDF of L is exerted by R_{pot} , followed by T_f and α , with the latter being more relevant for low recharge and small T_f . However, as α increases, the flowpaths become shallower, as evidenced by a larger occurrence of short pathways in the panels of the last column of Figure 3, and thereby the effect of recharge on the flowpath length distribution diminishes with respect to the fairly homogeneous formation of the first column.

The above results suggest that all the above factors influence the groundwater circulation, none dominating with respect to the others, though recharge remains the most relevant. Topography has a relatively small impact in a dry climate (red lines) compared to a wet climate (blue curves). Consequently, the commonly adopted geomorphological assumption that ties the distribution of catchment travel times to the width function of the basin does not hold for base flow, which is generated by groundwater and, as we showed above, is chiefly controlled by the interplay between recharge, topography, and distribution of hydraulic conductivity. It is not surprising, therefore, that the width function of the catchment, depicted in shaded gray in the upper right panel of Figure 3, deviates significantly from the simulated PDFs of the travel pathway lengths.

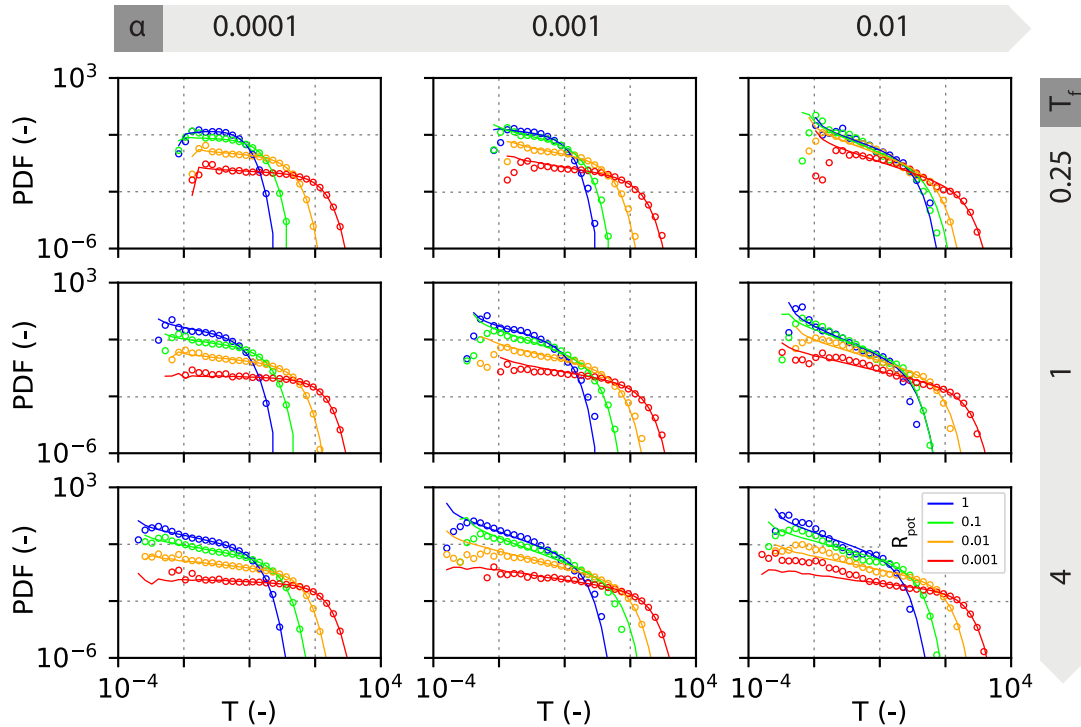


Figure 4. Probability Density Function of the dimensionless travel times for four selected dimensionless recharge rates (R_{pot}) and different values of α and T_f . The best-fitting Gamma distributions (Equation 8) are represented by solid lines. The results are for a formation depth of $D_i = 1000$ m (see Figure S3 in Supporting Information S1 for $D_i = 10$ m). The shape (a) and scale (b) parameters obtained by best fitting with the simulation results are shown in Table 2.

The travel time distribution is of paramount importance in catchment hydrology (Benettin et al., 2022). As observed by Kirchner et al. (2001) and further investigated by other authors (see, e.g., Benettin et al., 2022; Hrachowitz et al., 2010), the spectrum of the signal of a natural passive tracer traveling in a catchment decays similarly to that of the Gamma distribution

$$g(\tau) = \frac{\tau^{a-1}}{b^a \Gamma(a)} e^{-\tau/b} \quad (8)$$

where a and b are parameters and $\Gamma(a) = \int_0^\infty t^{a-1} e^{-t} dt$ is the Gamma function. The parameter a controls the shape of the PDF, and b is a scaling factor. Additional evidence of the flexibility offered by Equation 8 to represent the travel time distribution of a passive tracer at the hillslope scale is provided by Fiori and Russo (2008) and Alebachew et al. (2014) using hillslope scale flow simulations.

Figure 4 shows with solid lines the fitting of Equation 8 to the travel time distribution computed numerically as described in Section 2.3 and shown in the figure with open circles. The fitting parameters are summarized in Table 2. The Gamma distribution represents the variability of travel times well over the wide range of modeling parameters used in the simulations. The parameter a spans the range $0.36 \div 1.26$, with most of the values smaller than 1, but generally larger than the value of ~ 0.5 obtained by Kirchner et al. (2001) from the spectral analysis of the chloride time series in three small catchments along the Welsh coastline, UK. Humphrey et al. (2024) obtained values in the range $a = 0.4 \div 4.7$, and thereby in line with our analysis, by fitting Equation 8 to the experimental travel time distributions obtained from natural tracers analysis at several locations of the Upper Middle Loup watershed in the Northern High Plain aquifer, Nebraska (USA). For $a < 1$, the tail of the distribution declines more slowly than for the widely adopted exponential model (toward which the Gamma model (Equation 8) converges as $a \rightarrow 1$), highlighting the larger frequency of long residence times with respect to the exponential distribution.

Table 2
Parameters of the Gamma Distribution Obtained by Best Fitting of Equation 8 With the Simulated Travel Times Shown in Figure 4, for the Explored Values of R_{pot} , T_f and α

	R_{pot}	$\alpha = 0.0001$		$\alpha = 0.001$		$\alpha = 0.01$	
		a	b	a	b	a	b
$T_f = 0.25$	0.001	0.93	115.0	0.72	150.7	0.43	270.5
	0.01	0.90	13.2	0.71	17	0.39	33.9
	0.1	0.92	1.6	0.72	2.2	0.39	7.3
	1	1.26	0.4	0.93	0.8	0.51	5.8
$T_f = 1$	0.001	0.93	119.9	0.70	179.9	0.59	281.6
	0.01	0.83	19.2	0.60	28.8	0.48	41.5
	0.1	0.81	2.4	0.58	3.6	0.37	6.8
	1	0.82	0.5	0.57	0.8	0.36	2.5
$T_f = 4$	0.001	0.93	129.3	0.73	248.7	0.79	296.6
	0.01	0.82	25.7	0.56	62.4	0.65	61.5
	0.1	0.70	5.5	0.46	10.0	0.55	9.5
	1	0.66	1.2	0.41	2.2	0.43	2.5

The mean, variance, and skewness of the Gamma distribution are $\mu(T) = a b$, $\sigma^2(T) = a b^2$, and $SK = 2 a^{-1/2}$, respectively. Thus, considering the values of a and b reported in Table 2, we note that the mean travel time is chiefly controlled by b , as it varies more than a . Furthermore, SK scales inversely with a and is independent of b . In all cases, from wet to dry climates, both the mean and the standard deviation of the travel time increase by about two orders of magnitude as R_{pot} decreases from 1 to 0.001. The skewness, instead, shows a non-monotonous behavior with T_f . In a hilly topography ($T_f = 0.25$), it increases as R_{pot} decreases, while the opposite occurs for $T_f = 1$ and 4. In dry climates (small R_{pot}), a decreases from values close to 1 to about 0.5 as α increases, producing more skewed travel time distributions. Also, the mean travel times increase because the increase of b offsets the decrease of a . Consequently, the reduction of the Lagrangian velocity due to the stronger decline of hydraulic conductivity with depth for high α offsets the reduction of streamline lengths due to the larger frequency of shallow and short pathways, as shown in the third column of Figure 3. However, the larger variance and skewness associated with larger α values indicate a wider travel time distribution and a prevalence of long travel times as shown in Figure 4.

Figure 5 displays the Cumulative Distribution Function of the mean Lagrangian velocity, defined as the ratio between the length of the streamline and the corresponding travel time. Higher velocities are obtained with higher recharge and lower α . However, R_{pot} exerts the larger impact on the Lagrangian velocity, with the other parameters showing a smaller, yet appreciable, effect. In a dry climate ($R_{pot} = 0.001$), the Lagrangian velocity shows a broader range of variability than in a wetter climate ($R_{pot} = 0.1$), caused chiefly by a larger occurrence of small velocities. This combines with the

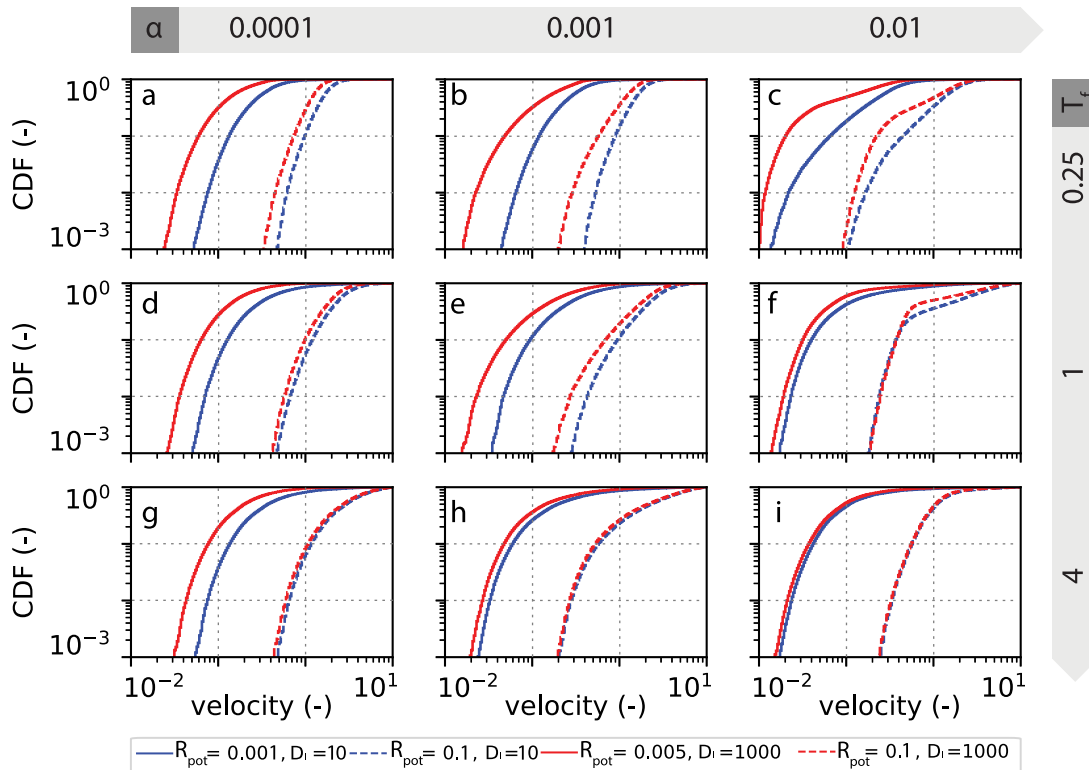


Figure 5. Cumulative Density Function of the dimensionless average Lagrangian velocity $|q|/(n K_G)$ of the streamlines under representative low and high recharge conditions (solid vs. dashed lines), shallow and deep formations (blue vs. red lines) and selected values of α and T_f .

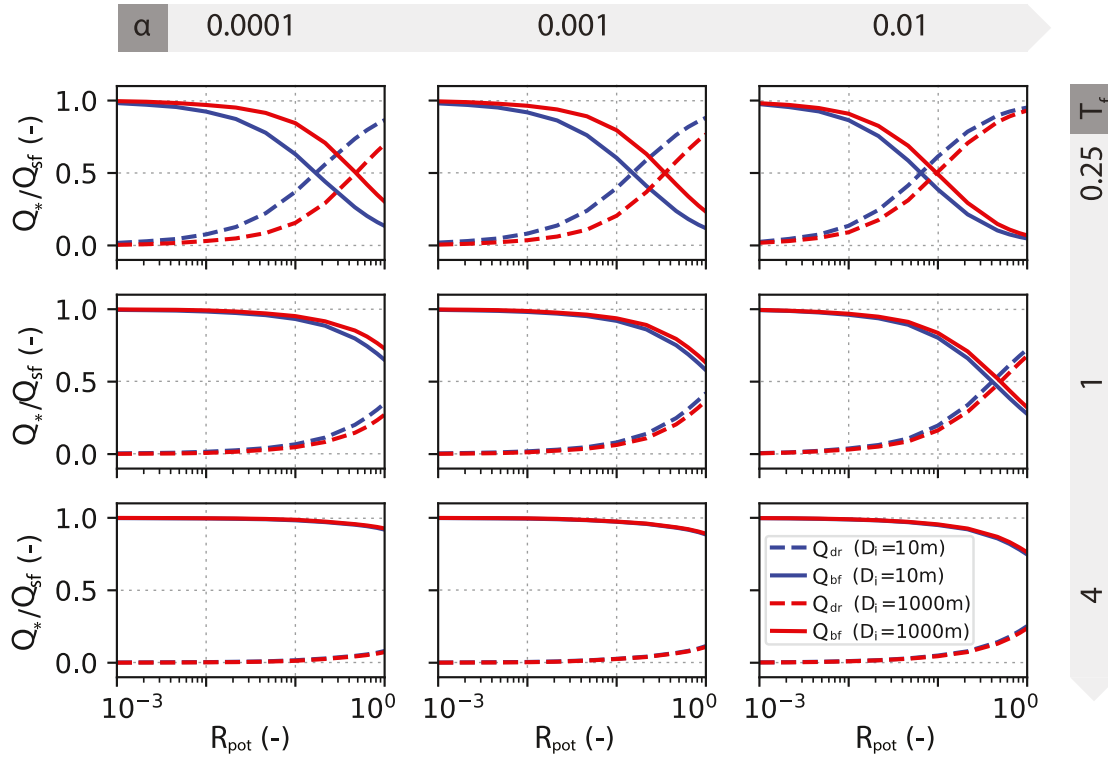


Figure 6. Share of the total outflow (i.e., the streamflow at the catchment outlet, Q_{sf}) generated as groundwater base flow (solid lines, Q_{bf}) as opposed to direct runoff (dashed lines, Q_{dr}) at increasing dimensionless recharge rates R_{pot} for different α , T_f and D_i values.

concurrent, though relatively less significant, increase of the flowpath lengths shown in Figure 3 to cause the remarkable growth of large travel times observed in Figure 4.

The long-term mean streamflow receives contributions from the groundwater and the direct runoff with a share quantified in Figure 6. Groundwater is the main contributor to streamflow at low recharge, but its share decreases as R_{pot} increases, and the water table rises approaching the land surface. At low relief ($T_f = 0.25$), the effect of D_i is evident, especially as recharge increases. However, the impact of D_i reduces as T_f increases, becoming negligible for $T_f = 4$, irrespective of R_{pot} . Similarly, α does not substantially influence the partitioning of streamflow between base flow and direct runoff when T_f is large. In summary, Figure 6 highlights how large α , low T_f , and shallow depths D_i promote the direct runoff, which progressively becomes a substantial share of the streamflow as potential recharge increases.

According to the adopted conceptualization, travel time distribution depends on (a) the partitioning of incoming potential recharge between quick direct runoff and groundwater base flow and (b) the age distribution of the base flow. Figure 7 (and Figure S4 in Supporting Information S1) shows how these two fluxes are modulated by the joint action of climate, as epitomized by R_{pot} , formation hydrogeology, through α and D_i , and morphology, through T_f . Streamflow age is generally negatively correlated with R_{pot} , mainly following a power law. Notably, as recharge increases, the topography becomes less pronounced and the subsurface less permeable (i.e., small T_f and large α), a larger share of stream water is generated as rapid runoff, which bypasses the groundwater flow system. As a result, the average streamflow age decreases. In the opposite conditions (low R_{pot} and α , or large T_f), streamflow is mostly fed by base flow, and its age mimics that of groundwater. Although streamflow age tends to increase with D_i , the effect is modest and mostly evident in mild topographies and/or relatively homogeneous hydraulic conductivity with depth (i.e., low α values).

Figure 8 shows the ratio V_{GW} between the groundwater volume above the elevation of the catchment's outlet and its maximum value v_{GW}^{\max} , where v_{GW}^{\max} is the water volume stored in the formation above the catchment's outlet. We

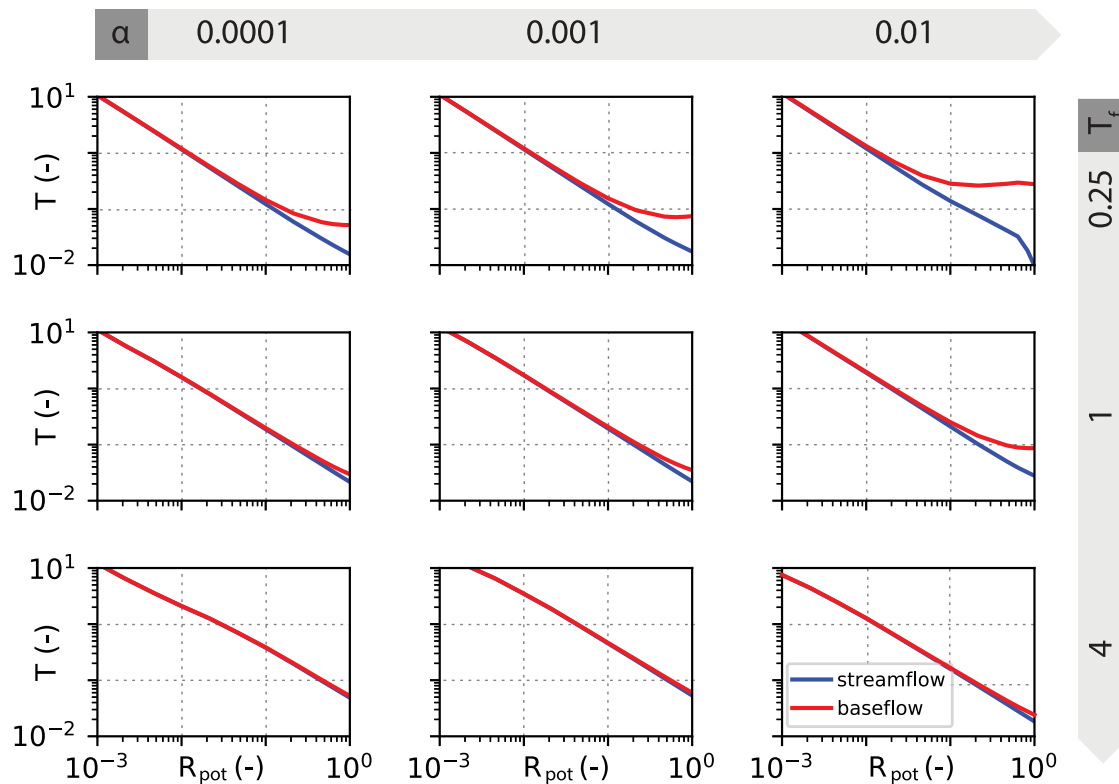


Figure 7. Comparison between the average age of streamflow and groundwater base flow under different geomorphoclimatic conditions. Streamflow comprises groundwater outflow and fast direct runoff (with zero age). The figure refers to $D_i = 1000$ m, see Figure S4 in Supporting Information S1 for $D_i = 10$ m.

consider this “drainable” volume as the most hydrogeologically active, though the groundwater stored at lower elevations may still be mobilized. At high relief (large T_f), deep formation (large D_i), and nearly homogeneous hydraulic conductivity (low α), a decrease of the recharge R_{pot} produces a sharp decrease of V_{GW} . Note that the active volume increases substantially with T_f as an effect of the larger available storage v_{GW}^{max} . This implies that, in absolute terms, the range of volumes stored in topographically rough settings can span an extensive range (i.e., the curves in an equivalent non-normalized plot would be very steep for large T_f). Furthermore, Figure 8 shows that the maximum available groundwater storage is reached for lower values of R_{pot} in the case of low reliefs as compared with high reliefs. In contrast, in the latter case, the maximum storage is reached only when K decays firmly with depth (i.e., for $\alpha = 10^{-2} \text{ m}^{-1}$). In general, increasing α produces a topographically constrained groundwater flow field, with the water table approaching the land surface in a progressively more significant portion of the catchment’s surface as R_{pot} increases, thereby increasing the groundwater volume and water residence time.

Figure 9 shows the spatial distribution of groundwater outflow and direct runoff at the catchment surface. The direct runoff is the portion of recharge that cannot enter the groundwater flow system because the water table is at the ground surface (see Section 2.2.2 and Figure 1d for details). Figure 9a shows that most of the catchment’s surface has zero outflows (yellow color). The remaining cells with fluxes larger than zero generate streamflow via subsurface base flow or as fast direct runoff. In the yellow parts of the catchment of Figure 9b recharge equals R_{pot} , whereas in the remaining areas the direct runoff equals the potential recharge (where groundwater is outflowing) or is in the range $[0, R_{pot}]$ where a fraction of R_{pot} should infiltrate to maintain the water table at the ground surface (see Section 2.2.2). The number of cells contributing to streamflow increases with recharge and decreases as T_f increases and/or α decreases. Considering that these maps refer to the long-term constant mean recharge, it can be concluded that higher relief catchments on permeable and homogeneous geologies tend to develop permanent river networks with lower drainage density than low relief catchments with a sharp decay of the hydraulic conductivity with depth. The same occurs when recharge decreases. Consequently, the drainage

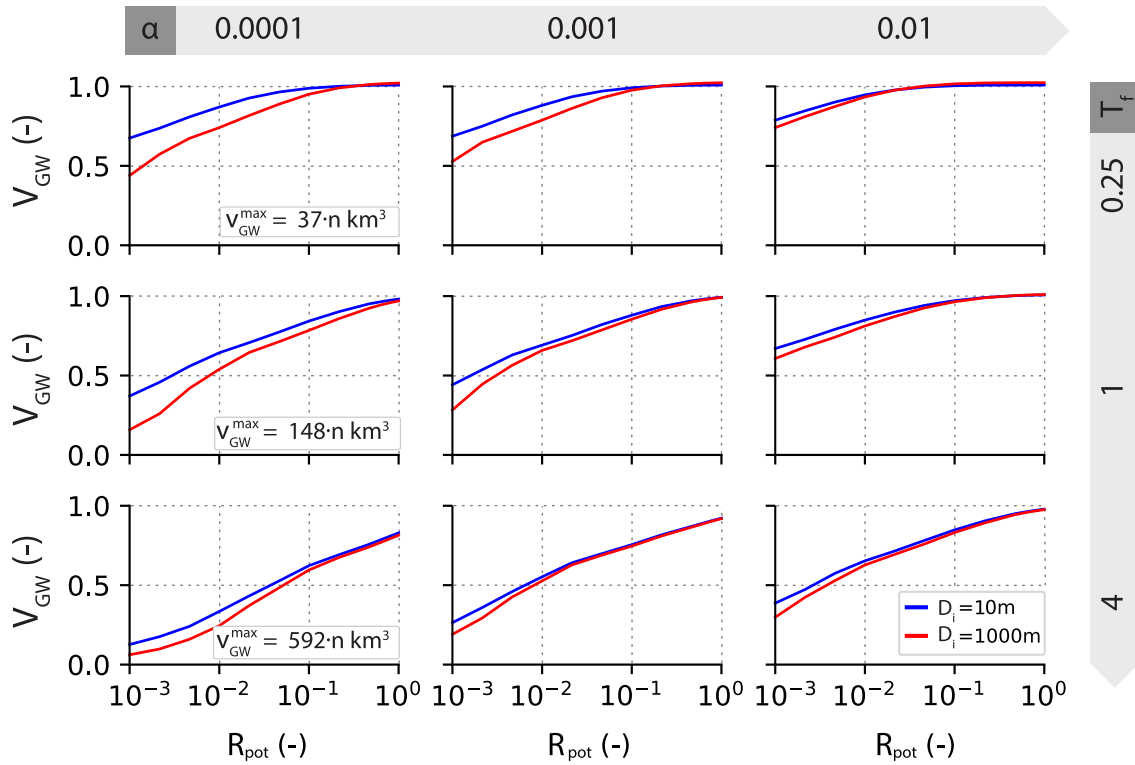


Figure 8. Volume of groundwater stored above the elevation of the catchment outlet, normalized by the total available storage V_{GW}^{\max} . The maximum available storage is reported on the left plots: it depends on catchment topography (controlled by T_f), and equals the formation's volume above the outlet multiplied by the porosity n .

density of the permanent river network, defined as the portion of the river network receiving a contribution from groundwater, decreases as the climate becomes drier, as expected, but also at high reliefs and in more permeable conditions. The former condition reflects the climate control of the hydrological system, and the latter the hydrogeomorphological control. Larger hydraulic conductivity at greater depths (i.e., low α) and large morphological gradients (i.e., large T_f) enhance deep water circulation, resulting in a flow field focused toward well-defined outflow areas in the lower portion of the drainage network. On the contrary, for larger values of α and hilly topography (i.e., low T_f), the ensuing shallow flow field feeds larger portions of the landscape with less intense specific flows.

Figure 10 shows the relationship between drainage density D_d of the permanent river network and the dimensionless catchment outflow $Q_{sf}/(K_G A)$. Drainage density is computed as the ratio between the catchment area where $q_{bf} > 0$ and the total area of the catchment. It identifies the portion of the surface drainage network persistently fed by groundwater. A power-law dependence $D_d = \lambda [Q_{sf}/(K_G A)]^\gamma$ emerges from Figure 10a, with the exponent γ varying between 0.65 and 0.72, thereby showing a consistent scaling over three orders of magnitude of $Q_{sf}/(K_G A)$ and across a wide range of geomorphoclimatic conditions. On the other hand, λ varies over a wider range: from $\lambda = 0.07$ for $T_f = 4$ and $\alpha = 0.0001 \text{ m}^{-1}$ to $\lambda = 2.54$, for $T_f = 0.25$ and $\alpha = 0.01 \text{ m}^{-1}$. Higher λ values denote the larger drainage densities that characterize low reliefs and sharp decays of K with depth (i.e., low T_f and high α), in agreement with the expansion of the network observed in Figure 9 under these conditions. Notice the cutoff of the power law scaling when the network approaches its maximum extent and the catchment is fully saturated. In this condition, any increase in streamflow is due to the fast direct runoff component, with the groundwater contribution remaining constant. This is observed for $T_f = 0.25$ and occurs at smaller values of $Q_{sf}/(K_G A)$ for higher α values because the stronger reduction of K with depth promotes shallower pathways that expand the saturated areas of the catchment.

Figure 10b (right) highlights the sensitivity of drainage density to the dimensionless catchment outflow and the parameter λ , which bears the signature of hydrogeological heterogeneity and topographic variability via α and T_f .

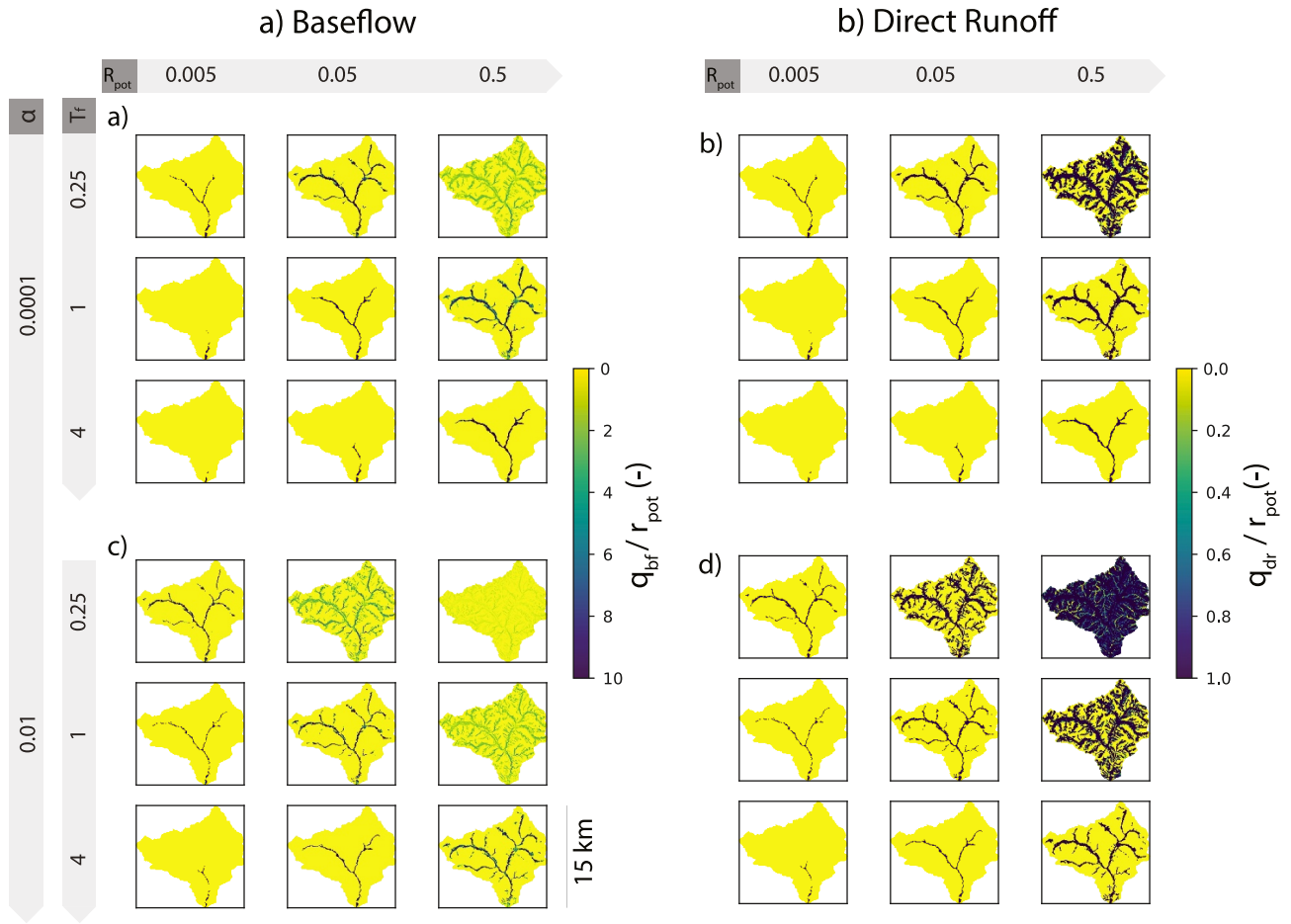


Figure 9. Spatial distribution of groundwater base flow (a) and direct runoff (b) fluxes (respectively, $q_{bf} = Q_{bf}/A_c$ and $q_{dr} = Q_{dr}/A_c$ as indicated in Section 2.2.2), normalized with respect to r_{pot} , under a few geomorphoclimatic conditions. All plots refer to $D_i = 1000$ m. Figure S5 in Supporting Information S1 shows the results for the full range of parameters considered in the present study. Figure S6 in Supporting Information S1 magnifies portions of the catchment where outflow is significant.

The sensitivity is quantified here as D'_d : the derivative of D_d with respect to $q_{sf} = Q_{sf}/(K_G A)$. In all settings, drainage density—and hence the total length of the stream network—is more sensitive to changes in q_{sf} under drier than wetter conditions (i.e., for lower q_{sf}). The large values of λ , associated with large α and/or low T_f , indicate a higher drainage density sensitivity to streamflow. Owing to the power law relationship between D_d and q_{sf} shown in Figure 10a, we notice that:

$$\frac{D'_d}{D_d} = \frac{\gamma}{q_{sf}}. \quad (9)$$

Hence, the normalized network density D'_d/D_d , and with it the drainage network extension, is inversely proportional to the dimensionless streamflow, given the remarkable consistent value of γ across all the explored scenarios (see Figure 10).

In addition, Figure 11 explores the relationship between the drainage density and the groundwater component of the streamflow. As the potential recharge increases, the relative contribution of groundwater to streamflow decreases. Nonetheless, drainage density increases, implying that the share of the catchment where groundwater contributes to streamflow increases as well. When the groundwater base flow is the main component of streamflow (i.e., for $Q_{bf}/Q_{sf} \approx 1$), drainage density and Q_{bf} are linearly related (1:1). On the other hand, for relatively wet conditions, low relief, and faster decay of K with depth (i.e., large R_{pot} , low T_f and high α), the

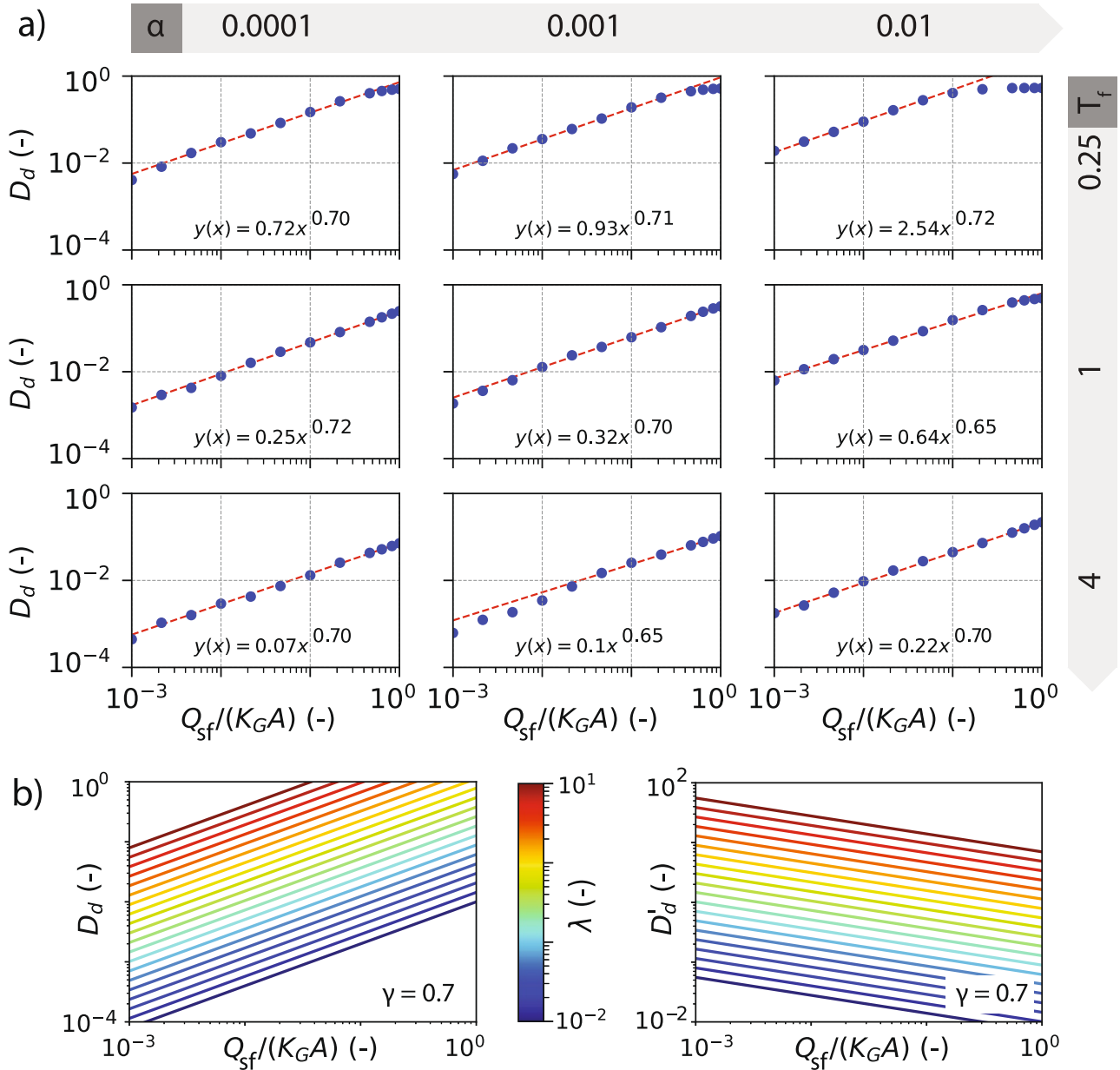


Figure 10. Relationship between drainage density D_d and normalized catchment outflow $Q_{sf}/(K_G A)$ across the range of studied geomorphoclimatic conditions. (a) Modeled results (bullets) and best fitting power law $D_d = \lambda(Q_{sf}/(K_G A))^\gamma$ (solid lines; the fitting is limited to $Q_{sf}/(K_G A) < 0.1$ in case of $T_f = 0.25$); (b) Range spanned by the D_d versus $Q_{sf}/(K_G A)$ relationships (left) and its derivative D'_d (right), as a function of λ for a fixed $\gamma = 0.7$. The results are for $D_i = 1000$ m. Similar results for $D_i = 10$ m are shown in the Figure S7 in Supporting Information S1.

relationship flattens, with approximately half of the catchment discharging groundwater while the remaining half is recharged.

4. Discussion

A first characteristic of the subsurface flow in a mountainous region is the distribution of flowpaths lengths as a function of the climatic, morphological, and hydrogeological drivers. The climate driver, epitomized here by R_{pot} , exerts the major effect on the length of the flowpaths. Higher recharge causes the water table to rise and promotes short pathways, while the long ones become relatively less frequent (Figure 3). This effect is more noticeable in

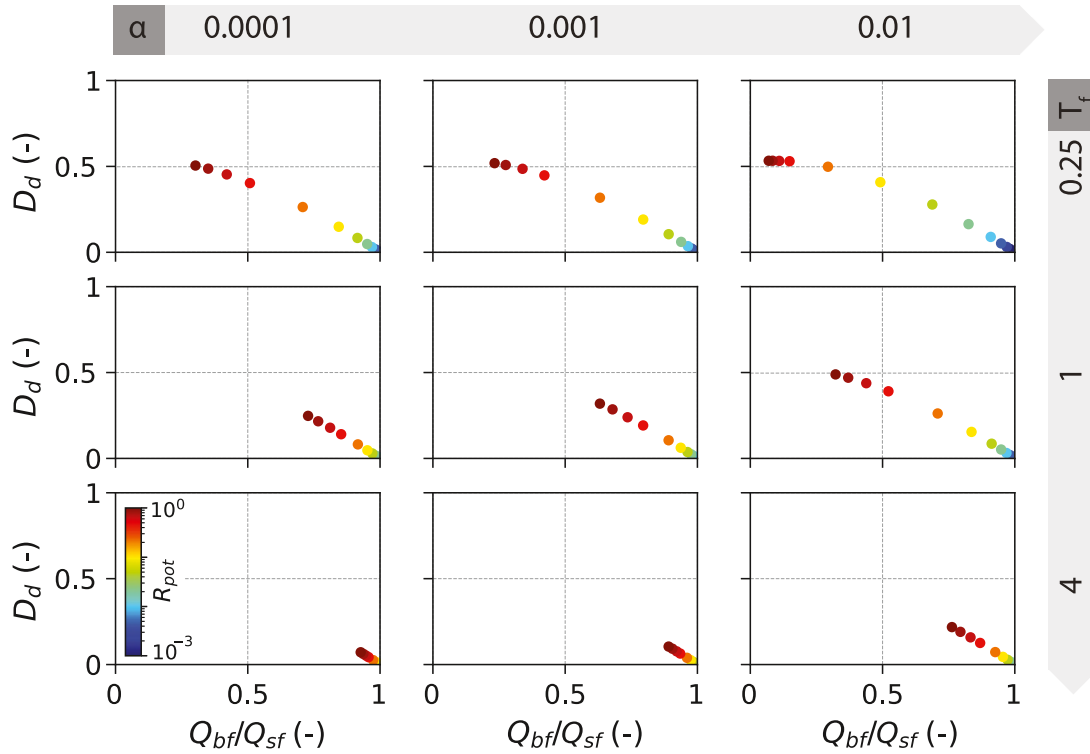


Figure 11. Relationship between drainage density D_d and normalized catchment base flow $Q_{bf}/(K_G A)$ across the range of studied geomorphoclimatic conditions. The results are for $D_i = 1000$ m; for $D_i = 10$ m see Figure S8 in Supporting Information S1.

low than in high-relief catchments, as the larger storage volume of the latter prevents the water table from reaching the ground surface, even when R_{pot} is large (see Figures 8 and 9). Similarly, the occurrence of short pathways increases with α at the expense of a less than proportional decrease in the occurrence of long flowpaths. The impact of α on the flowpaths length is smaller than that of R_{pot} and is affected by the uncertainty inherited from the hydrogeological conceptual model. In the pursuit of generality, we neglected site-specific features such as faults, with the decline of the hydraulic conductivity with depth as the only feature included in the hydrogeological model of heterogeneity. Nonetheless, the conceptualization adopted in this study agrees with the hydrogeological structure of most mountain formations outlined by Welch and Allen (2014), and it is widely adopted in the literature (see, e.g., Ameli et al., 2016; Wörman et al., 2007). Moreover, despite the uncertainty affecting local flows due to the unknown and, therefore, unrepresented variations of the hydraulic properties, the relatively mild effect of α on the overall flow characteristics confers robustness to the general conclusions drawn by using this model of spatial variability.

Given that long flowpaths develop with higher head differences, the Lagrangian velocity varies less for higher R_{pot} values (i.e., about three orders of magnitude for $R_{pot} = 0.05$ and one order of magnitude for $R_{pot} = 0.5$, Figure 5), with respect to travel times which span about six orders of magnitude (see Figure 4). In addition, α exerts a smaller effect on the travel time distribution than on the flowpath length. This is because the compaction of the streamlines toward the surface at large α partially compensates for the reduction of K with depth. As a consequence, α modulates the reduced variability in the travel time distribution shown in Figure 4 as compared to the distribution of the flowpath length of Figure 3. Thus, the flowpaths adjust to the vertical distribution of hydraulic conductivity, causing changes in travel times that are less than proportional to changes in α .

A closer inspection of Figure 2a reveals that the travel times decrease as α increases for $T_f = 0.25$, but the opposite occurs for $T_f = 4$. This behavior can be explained by the interplay between two competing factors on travel times caused by the reduction of K with depth. On one side, the reduction of K increases the travel times of deep flowpaths, as they encounter a higher flow resistance. On the other, the frequency of deep flowpaths reduces in favor of shallow, short, and quick flowpaths. The first effect prevails for high reliefs ($T_f = 4$), whereas the

second one prevails for hilly reliefs ($T_f = 0.25$). Figure 3 shows that an increase of α has a minor effect on the PDF of the flowpath lengths for $T_f = 4$, suggesting that a significant share of flowpaths reaches large depths despite the reduced permeability. Indeed, when topographic variability increases (i.e., for large T_f), the water table can rise further as a consequence of the additional storage volume available (see Figure 8). The resulting high hydraulic gradients can ultimately push a significant amount of water toward deeper and less conductive regions of the flow domain, compensating for the effect of the sharper decline of the hydraulic conductivity with depth. Deep flows that are promoted by a vertically extended domain (e.g., by large values of either T_f or D_i) or by hydraulically conductive formations (by either large K_G or low α) contribute to focus base flow outflows toward the most downstream topographic incisions. As conceptualized in this study, the quick runoff component is also restricted to these areas, as elsewhere the water table is deep enough to accommodate the incoming recharge (see Figure 9 and Figure S3 in Supporting Information S1). In these conditions, groundwater outflows are substantial: they are spatially focused and prevail over quick, direct runoff, as most recharge infiltrates. On the opposite end of low T_f or D_i and low K_G or large α , groundwater outflows will be less intense and more diffused across the catchment. The direct runoff will also be triggered more diffusely, reaching its upper limit R_{pot} more extensively across the catchment. All the previous aspects are further modulated by the incoming potential recharge, which bears the climatic signature on the simulated scenarios.

Because of the shallow water table, catchments experiencing more diffuse long-term groundwater base flow are more prone to respond quickly to short-term meteorological inputs, leading to flashy runoff responses. These conditions will favor superficial/shallow runoff and short concentration times. On the contrary, when the water table is at a greater depth, the sizable available storage can buffer meteorological forcing, favoring downstream persistent flow regimes. This character of mountain aquifers was empirically observed by Carlston (1963) and is confirmed here.

Catchments experiencing diffused base flow might be less sensitive to climatic alterations. In fact, in these settings, the flow field is topographically constrained and—as Figure 8 shows—the storage volumes (and hence the groundwater configuration) show limited variability with R_{pot} . On the other hand, the fast direct runoff is expected to be more sensitive to climate change than the base flow, given its higher sensitivity to the water table elevation. Conversely, in geomorphoclimatic conditions where surface topography and water table are decoupled, a reduced recharge will mostly impact the groundwater component of the hydrological response.

Climate change is anticipated to raise average temperatures in many regions worldwide, resulting in more intense precipitation due to the increased energy of the atmosphere and its enhanced capacity to hold water vapor (Adler et al., 2022). In this scenario, the larger evapotranspiration (due to higher temperatures) and the fast shallow/superficial runoff (generated by more intense rainfalls) will likely reduce groundwater recharge, especially in mountain aquifers characterized by relatively low hydraulic conductivities. Consequently, base flows are expected to decrease, and the extent of the perennial river network to shrink, starting from the lower-order streams at higher elevations (Figure 9). Nonetheless, thanks to the slower and deeper groundwater flow that feeds river networks under drier conditions (Figure 2), the base flow becomes more resilient to climate change and less variable downstream. Furthermore, when the recharge decreases, streams will be progressively fed by a larger fraction of deep groundwater, causing the streamflow age to increase (Figure 7), possibly affecting water biochemical composition. Such changes in the hydrological cycle under a drying climate with a lower R_{pot} are expected to occur at the expense of groundwater storage, which may suffer a significant reduction (Figure 8). As ample water storage (v_{GW}^{max}) is available when deep valleys surround prominent topographic reliefs, mountainous environments have the potential to better buffer long-term climatic variability from the hydrological perspective as compared to hilly areas. Although the mountainous environment can be characterized by a reduced drainage density, the sensitivity of drainage density to recharge alterations is smaller compared to hilly areas (Figure 10b). On the contrary, hilly landscapes are characterized by larger drainage densities. Nonetheless, a reduction in recharge driven by climatic alterations may greatly impact the extent of the permanent drainage network, which shrinks substantially as the water table decouples from the surface topography (Figure 10b and Equation 9). Shrinking drainage networks can have dramatic consequences on riverine ecology (Jaeger et al., 2014) as, for example, drainage density controls the link between spatially distributed biogeochemical processes acting on the hillslopes and the riparian and riverine functioning guaranteed by hydrological connectivity along the drainage network (Mari et al., 2014; Rinaldo et al., 2018; Tonkin et al., 2018). With a progressive shrinkage of the persistent stream network, riverine ecosystems will be forced downstream, altering the ecohydrological status of

upstream areas. Interestingly, the factor λ alone bears the signature of the climatic and hydromorphological variability considered in this study on the relationship between drainage density and streamflow (Figure 10). At the same time, the scaling exponent γ remains relatively constant.

5. Conclusions

We analyzed the primary hydro-geomorphoclimatic controls on base flow in a mountainous region with topography ranging from hilly to rugged. The sensitivity of groundwater travel times, flowpath lengths, and streamflow age are explored as a function of climate, as epitomized by groundwater recharge, surface morphology, and vertical distribution of hydraulic conductivity. In addition, we investigated groundwater storage, the partitioning of recharge into the base flow and direct runoff, the spatial variability of such fluxes, and the drainage density of the permanent river network fed by groundwater.

This study highlights the relative importance of the geomorphoclimatic drivers that control the slow hydrological response in mountain regions and how they interact in non-linear and non-trivial ways. The distribution of the subsurface flowpath lengths does not conform to the width function obtained from surface morphology alone. In addition, a power-law dependence, modulated by topography and subsurface hydraulic conductivity, has been identified between the travel time distribution and potential recharge (controlled by climate) across several orders of magnitudes, with a cutoff placed where the subsurface flow becomes topographically bounded. A power law with a consistent scaling exponent also emerges between drainage density and streamflow.

The depth at which the groundwater flow system develops is an important controlling factor of the hydrological response of catchments to climatic input and alterations. Shallow flows that develop preferentially in hilly topography with high recharge increase the occurrence of fast flowpaths, producing hillslope-driven runoff responses. On the other hand, deeper flows that develop preferentially in high relief areas with a relatively small recharge promote the development of complex nested circulation patterns in the subsurface and inter-catchment flows.

The depth reached by subsurface circulation is enhanced by large and homogeneous hydraulic conductivity, by topographical variability, and formation depth. In such conditions, surface drainage density is low, and groundwater base flow is intense and focused along the primary topographical incisions (where a modest amount of quick, direct runoff is also generated). Decreasing recharge will lower the water table, reduce subsurface storage, and increase the water age and the fraction of the base flow generated by groundwater. This causes the permanently active drainage network to shrink and move downstream, further reducing the surface drainage density, thereby ultimately limiting the extension of riverine and riparian habitats. However, it will also enhance the buffer capacity of the catchment against changes in precipitation, potentially increasing the resilience of the remaining groundwater-fed part of the drainage network to further climatic alterations. In these situations, streamflow age will increase, approaching that of groundwater base flow. Longer flowpaths and travel times and slower flow velocities are likely to impact the thermodynamic behavior of surface waters and their biochemical composition (e.g., improving water quality or increasing the concentration of dissolved geogenic species). In the opposite conditions (i.e., wet climate, low topographical variability, low and sharply depth-decaying hydraulic conductivity, and shallow formation depths), low-intensity base flows will persistently feed a larger share of the topographic incisions, ultimately increasing surface drainage density. Quick runoff will also be triggered more frequently and extensively across the catchment, possibly enhancing short-term runoff dynamics, sediment transport, and soil erosion. In these settings, the stream water age will be younger than that of the surrounding aquifers, with the potential risk of contamination of surface waters from diffuse leaching of pollutants from the surficial soil layer. Furthermore, the fast component of the hydrological response might suffer alterations in the context of a changing climate, as the spatial distribution of recharge and its partitioning into groundwater and quick flows is more sensitive to recharge than to other controlling factors.

In recharge-controlled groundwater systems, consistent scaling relations tie recharge with critical variables that describe the hydrological functioning of the system, such as base flow, ultimately increasing confidence in the system's response to various climatic scenarios. Conversely, tipping points and non-linear responses may arise in topography-controlled groundwater flow systems, mainly when recharge changes couple or decouple the water table from the ground surface. Under these conditions, the hydrological system can become more vulnerable to climate change, with the resulting impacts more challenging to predict.

Climatic alterations are expected to impact the ecohydrological functioning of river networks, as rising temperatures will likely reduce groundwater recharge and, in turn, surface drainage density. However, the impacts on ecosystem services linked to the extent of the persistently active drainage network are expected to be modulated by different morphological, geological, and climatic traits, as this study contributed to quantify.

The current study has limitations tied to the modeling assumptions, which unavoidably simplify a complex system. These include (a) the stationary flow hypothesis, (b) the simplified subsurface heterogeneity model, (c) the model geometry, particularly the assumption of lateral non-flow boundaries at the catchment's divide and at the outlet, (d) the application of the recharge directly on the water table without considering the unsaturated zone, which is the main reason why we considered a long term mean aquifer recharge.

Finally, it is worth highlighting that, despite steady-state simulations are not suitable for reproducing short-term dynamics, the wide range of recharge scenarios considered in the present study can provide valuable clues on the evolution of the system under long-term climatic variability, assuming that they can be approximated as a sequence of steady states.

Notation

\mathbf{x} [L]	Spatial coordinates
$z(\mathbf{x})$ [L]	Ground surface elevation
$\eta(x_1, x_2)$ [L]	Water table elevation
h [L]	Hydraulic head
T_f [–]	Vertical topographic stretch factor
α [L^{-1}]	Vertical decay rate of the hydraulic conductivity
D_i [L]	Vertical extent of the flow domain below the catchment outlet
n	porosity
$K(\mathbf{x})$ [LT^{-1}]	Hydraulic conductivity
K_G [LT^{-1}]	Hydraulic conductivity at the ground surface
$k(\mathbf{x}; \alpha)$ [–]	Dimensionless function controlling the depth-decay of K
A [L^2]	Catchment area
A_c [L^2]	Horizontal area of the cells of the numerical model
l [L]	Characteristic spatial scale ($l = \sqrt{A}$)
$n l / K_G$ [T]	Characteristic Lagrangian timescale
r_{pot} [LT^{-1}]	Potential recharge
r [LT^{-1}]	Actual recharge
R_{pot} [–]	Potential dimensionless recharge (r_{pot} / K_G)
R [–]	Actual dimensionless recharge (r / K_G)
q_{bf} [LT^{-1}]	Local base flow specific flux (i.e., groundwater outflow)
$Q_{bf, i}$ [$L^3 T^{-1}$]	Local base flow discharge at the surface seepage cell i
Q_{bf} [$L^3 T^{-1}$]	Total base flow discharge
q_{dr} [LT^{-1}]	Local direct runoff specific flux (i.e., fast hydrological response)
$Q_{dr, i}$ [$L^3 T^{-1}$]	Local direct runoff discharge at surface cell i
Q_{dr} [$L^3 T^{-1}$]	Total direct runoff discharge

Q_{sf} [$L^3 T^{-1}$]	Streamflow at the catchment outlet ($Q_{sf} = Q_{bf} + Q_{dr}$)
q_{sf} [-]	Specific dimensionless streamflow at the catchment outlet ($q_{sf} = Q_{sf}/(K_G A)$)
N_p [-]	Maximum number of particles released for each cell where $r > 0$
CD [$L^2 T^{-1}$]	Drain conductance in the MODFLOW DRN package
$g(\tau)$ [T^{-1}]	Gamma distribution
$\Gamma(a)$ [-]	Gamma function
a [-]	Scale parameter of the Gamma distribution
b [T]	Rate parameter of the Gamma distribution
v_{GW}^{max} [L^3]	Maximum storable groundwater volume
$V_{GW} = \frac{v_{GW}}{v_{max_{GW}}} [-]$	Dimensionless storage volume
D_d [L^{-1}]	Drainage density
$Q_{sf}/(K_G A)$ [-]	Dimensionless streamflow (i.e., catchment outflow)
λ [L^{-1}]	Factor relating drainage density and dimensionless streamflow
γ [-]	Exponent relating drainage density and the dimensionless streamflow

Data Availability Statement

All data were generated through simulations performed using MODFLOW-NWT (Niswonger et al., 2011) and MODPATH Version 7 (Pollock, 2016), both available under Public Domain license at <https://www.usgs.gov/software/modflow-nwt-a-newton-formulation-modflow-2005> and <https://www.usgs.gov/software/modpath-particle-tracking-model-modflow>, respectively. The respective models were built using the Python package FloPy (Bakker et al., 2024; Leaf & Fienen, 2022) available under the BSD 3-Clause license and published on GitHub at <https://doi.org/10.5066/F7BK19FH>. Figures were made with Matplotlib version 3.2.1 (Caswell et al., 2020; Hunter, 2007), available under the Matplotlib license at <https://matplotlib.org/>. The Python Notebook used to build the models is available under the MIT license and published on Zenodo (Betterle, 2024) <https://doi.org/10.5281/zenodo.13350627>. The Notebook contains the Digital Elevation Map of the reference catchment available under the Creative Commons (CC BY 2.5 IT) license from the WebGis of the Autonomous Province of Trento (Ufficio Sistemi Informativi - Servizio autorizzazioni e valutazioni ambientali, 2013) at <https://siat.provincia.tn.it/stem/>.

References

- Abe, Y., Uchiyama, Y., Saito, M., Ohira, M., & Yokoyama, T. (2020). Effects of bedrock groundwater dynamics on runoff generation: A case study on granodiorite headwater catchments, western Tanzawa Mountains, Japan. *Hydrological Research Letters*, 14(1), 62–67. <https://doi.org/10.3178/hrl.14.62>
- Adler, C., Wester, P., Bhatt, I., Huggel, C., Insarov, G., Morecroft, M., et al. (2022). Cross-chapter paper 5: Mountains. In H. O. Pörtner, D. C. Roberts, C. H. Trisos, N. P. Simpson, V. Möller, C. Méndez, et al. (Eds.), *Climate change 2022: Impacts, adaptation and vulnerability. contribution of working group ii to the sixth assessment report of the intergovernmental panel on climate change* (pp. 2273–2318). Cambridge University Press. <https://doi.org/10.1017/9781009325844.022>
- Alebachev, M. A., Fiori, A., & Russo, D. (2014). A comparison of travel-time based catchment transport models, with application to numerical experiments. *Journal of Hydrology*, 511, 605–618. <https://doi.org/10.1016/j.jhydrol.2014.02.010>
- Ameli, A. A., McDonnell, J. J., & Bishop, K. (2016). The exponential decline in saturated hydraulic conductivity with depth: A novel method for exploring its effect on water flow paths and transit time distribution. *Hydrological Processes*, 30(14), 2438–2450. <https://doi.org/10.1002/hyp.10777>
- Bakker, M., Post, V., Hughes, J. D., Langevin, C., White, J. T., Leaf, A., et al. (2024). Flopy v3.9.0.dev0 [Software]. *Zenodo*. <https://doi.org/10.5066/F7BK19FH>
- Battin, T. J., Lauerwald, R., Bernhardt, E. S., Bertuzzo, E., Gener, L. G., Hall, R. O., et al. (2023). River ecosystem metabolism and carbon biogeochemistry in a changing world. *Nature*, 613(7944), 449–459. <https://doi.org/10.1038/s41586-022-05500-8>
- Benettin, P., Rodriguez, N. B., Sprenger, M., Kim, M., Klaus, J., Harman, C. J., et al. (2022). Transit time estimation in catchments: Recent developments and future directions. *Water Resources Research*, 58(11), e2022WR033096. <https://doi.org/10.1029/2022WR033096>

Acknowledgments

Alberto Bellin acknowledges funding by the PNRR project iNEST (Interconnected NordEst Innovation Ecosystem), Mission 4.2, Investment 1.5, NextGeneration EU (Project ID: ECS 00000043, Digital, Industry, Aerospace). Open access publishing facilitated by Università degli Studi di Trento, as part of the Wiley - CRUI-CARE agreement.

- Benettin, P., Soulsby, C., Birkel, C., Tetzlaff, D., Botter, G., & Rinaldo, A. (2017). Using SAS functions and high-resolution isotope data to unravel travel time distributions in headwater catchments. *Water Resources Research*, 53(3), 1864–1878. <https://doi.org/10.1002/2016WR020117>
- Berkowitz, B., & Zehe, E. (2020). Surface water and groundwater: Unifying conceptualization and quantification of the two “water worlds”. *Hydrology and Earth System Sciences*, 24(4), 1831–1858. <https://doi.org/10.5194/hess-24-1831-2020>
- Betterle, A. (2024). Mountain_aquifers_v1 [ComputationalNotebook]. Zenodo. <https://doi.org/10.5281/zenodo.1335067>
- Botter, G., Bertuzzo, E., Bellin, A., & Rinaldo, A. (2005). On the Lagrangian formulations of reactive solute transport in the hydrologic response. *Water Resources Research*, 41(4), W04008. <https://doi.org/10.1029/2004WR003544>
- Botter, G., Bertuzzo, E., & Rinaldo, A. (2011). Catchment residence and travel time distributions: The master equation. *Geophysical Research Letters*, 38(11), L11403. <https://doi.org/10.1029/2011GL047666>
- Caine, J. S. (2006). *Questa baseline and pre-mining ground-water quality investigation 18. Characterization of brittle structures in the Questa Caldera and their potential influence on bedrock ground-water flow, Red River Valley, New Mexico*. US Geological Survey. Retrieved from <https://pubs.usgs.gov/pp/2006/1729/>
- Caine, J. S., & Tomasiak, S. R. (2003). Brittle structures and their role in controlling porosity and permeability in a complex Precambrian crystalline-rock aquifer system in the Colorado Rocky Mountain Front Range. *Geological Society of America Bulletin*, 115(11), 1410–1424. <https://doi.org/10.1130/B25088.1>
- Camporese, M., Paniconi, C., Putti, M., & Orlandini, S. (2010). Surface-subsurface flow modeling with path-based runoff routing, boundary condition-based coupling, and assimilation of multisource observation data. *Water Resources Research*, 46(2), W02512. <https://doi.org/10.1029/2008WR007536>
- Carlston, C. W. (1963). *Drainage density and streamflow* (Technical Report) (p. 20402). US Government Printing Office.
- Caswell, T. A., Droettboom, M., Lee, A., Hunter, J., Firing, E., Stansby, D., et al. (2020). matplotlib/matplotlib v3.2.1 [Software]. Zenodo. <https://doi.org/10.5281/zenodo.3714460>
- Clark, M. P., Fan, Y., Lawrence, D. M., Adam, J. C., Bolster, D., Gochis, D. J., et al. (2015). Improving the representation of hydrologic processes in Earth system models. *Water Resources Research*, 51(8), 5929–5956. <https://doi.org/10.1002/2015WR017096>
- Condon, L. E., Markovich, K. H., Kelleher, C. A., McDonnell, J. J., Ferguson, G., & McIntosh, J. C. (2020). Where is the bottom of a watershed? *Water Resources Research*, 56(3), e2019WR026010. <https://doi.org/10.1029/2019WR026010>
- Cvetkovic, V., Carstens, C., Selroos, J.-O., & Destouni, G. (2012). Water and solute transport along hydrological pathways. *Water Resources Research*, 48(6), W06537. <https://doi.org/10.1029/2011WR011367>
- Cvetkovic, V., & Dagan, G. (1994). Transport of kinetically sorbing solute by steady random velocity in heterogeneous porous formations. *Journal of Fluid Mechanics*, 265, 189–215. <https://doi.org/10.1017/S00222112094000807>
- Dagan, G. (1989). *Flow and transport on porous formations*. Springer.
- de Graaf, I. E. M., Sutanudjaja, E. H., van Beek, L. P. H., & Bierkens, M. F. P. (2015). A high-resolution global-scale groundwater model. *Hydrology and Earth System Sciences*, 19(2), 823–837. <https://doi.org/10.5194/hess-19-823-2015>
- Di Dato, M., Bellin, A., Cvetkovic, V., Dagan, G., Dietrich, P., Fiori, A., et al. (2023). Baseflow statistics in aggregated catchments. *Water Resources Research*, 59(12), e2023WR035894. <https://doi.org/10.1029/2023WR035894>
- Fan, Y., Clark, M., Lawrence, D. M., Swenson, S., Band, L. E., Brantley, S. L., et al. (2019). Hillslope hydrology in global change research and earth system modeling. *Water Resources Research*, 55(2), 1737–1772. <https://doi.org/10.1029/2018WR023903>
- Fiori, A., & Russo, D. (2007). Numerical analyses of subsurface flow in a steep hillslope under rainfall: The role of the spatial heterogeneity of the formation hydraulic properties. *Water Resources Research*, 43(7), W07445. <https://doi.org/10.1029/2006WR005365>
- Fiori, A., & Russo, D. (2008). Travel time distribution in a hillslope: Insight from numerical simulations. *Water Resources Research*, 44(12), W12426. <https://doi.org/10.1029/2008WR007135>
- Forster, C., & Smith, L. (1988a). Groundwater flow systems in mountainous terrain: 1. Numerical modeling technique. *Water Resources Research*, 24(7), 999–1010. <https://doi.org/10.1029/WR024i007p00999>
- Forster, C., & Smith, L. (1988b). Groundwater flow systems in mountainous terrain: 2. Controlling factors. *Water Resources Research*, 24(7), 1011–1023. <https://doi.org/10.1029/WR024i007p01011>
- Gleeson, T., & Manning, A. H. (2008). Regional groundwater flow in mountainous terrain: Three-dimensional simulations of topographic and hydrogeologic controls. *Water Resources Research*, 44(10), W10403. <https://doi.org/10.1029/2008WR006848>
- Gonfiantini, R., Fröhlich, K., Araguás-Araguás, L., & Rozansky, K. (1998). Isotopes in groundwater hydrology. In C. Kendall & J. J. McDonnell (Eds.), *Isotope tracers in catchment hydrology*. Elsevier.
- Grant, G. E., & Dietrich, W. E. (2017). The frontier beneath our feet. *Water Resources Research*, 53(4), 2605–2609. <https://doi.org/10.1002/2017WR020835>
- Hahm, W. J., Dralle, D. N., Sanders, M., Bryk, A. B., Fauria, K. E., Huang, M. H., et al. (2022). Bedrock vadose zone storage dynamics under extreme drought: Consequences for plant water availability, recharge, and runoff. *Water Resources Research*, 58(4), e2021WR031781. <https://doi.org/10.1029/2021WR031781>
- Harbaugh, A. (2005). MODFLOW-2005, the U.S. Geological Survey modular ground-water model – The Ground-water flow process. *U.S. Geological Survey Techniques and Methods 6-A16* (Technical Report). Retrieved from <https://pubs.usgs.gov/tm/2005/tm6A16/>
- Hawker, L., Uhe, P., Paulo, L., Sosa, J., Savage, J., Sampson, C., & Neal, J. (2022). A 30 m global map of elevation with forests and buildings removed. *Environmental Research Letters*, 17(2), 024016. <https://doi.org/10.1088/1748-9326/ac4d4f>
- Hayashi, M. (2020). Alpine hydrogeology: The critical role of groundwater in sourcing the headwaters of the world. *Groundwater*, 58(4), 498–510. <https://doi.org/10.1111/gwat.12965>
- Hrachowitz, M., Soulsby, C., Tetzlaff, D., Malcolm, I. A., & Schoups, G. (2010). Gamma distribution models for transit time estimation in catchments: Physical interpretation of parameters and implications for time-variant transit time assessment. *Water Resources Research*, 46(10), 15. <https://doi.org/10.1029/2010WR009148>
- Humphrey, C. E., Solomon, D. K., Gilmore, T. E., MacNamara, M. R., Genereux, D. P., Mittelstet, A. R., et al. (2024). Spatial variation in transit time distributions of groundwater discharge to a stream overlying the northern High Plains Aquifer, Nebraska, USA. *Water Resources Research*, 60(2), e2022WR034410. <https://doi.org/10.1029/2022WR034410>
- Hunter, J. D. (2007). Matplotlib: A 2D graphics environment. *Computing in Science & Engineering*, 9(3), 90–95. <https://doi.org/10.1109/MCSE.2007.55>
- Huss, M., Bookhagen, B., Huggel, C., Jacobsen, D., Bradley, R., Clague, J., et al. (2017). Toward mountains without permanent snow and ice. *Earth's Future*, 5(5), 418–435. <https://doi.org/10.1002/2016EF000514>
- IEA. (2021). *Hydropower data explorer* (Technical Report). IEA. Retrieved from <https://www.iea.org/data-and-statistics/data-tools/hydropower-data-explorer>

- Immerzeel, W. W., Lutz, A. F., Andrade, M., Bahl, A., Biemans, H., Bolch, T., et al. (2020). Importance and vulnerability of the world's water towers. *Nature*, 577(7790), 364–369. <https://doi.org/10.1038/s41586-019-1822-y>
- Immerzeel, W. W., van Beek, L. P. H., & Bierkens, M. F. P. (2010). Climate change will affect the Asian water towers. *Science*, 328(5984), 1382–1385. <https://doi.org/10.1126/science.1183188>
- Jaeger, K. L., Olden, J. D., & Pelland, N. A. (2014). Climate change poised to threaten hydrologic connectivity and endemic fishes in dryland streams. *Proceedings of the National Academy of Sciences*, 111(38), 13894–13899. <https://doi.org/10.1073/pnas.1320890111>
- Jencso, K. G., McGlynn, B. L., Gooseff, M. N., Wondzell, S. M., Bencala, K. E., & Marshall, L. A. (2009). Hydrologic connectivity between landscapes and streams: Transferring reach- and plot-scale understanding to the catchment scale. *Water Resources Research*, 45(4), W04428. <https://doi.org/10.1029/2008WR007225>
- Käser, D., & Hunkeler, D. (2016). Contribution of alluvial groundwater to the outflow of mountainous catchments. *Water Resources Research*, 52(2), 680–697. <https://doi.org/10.1002/2014WR016730>
- Katsura, S., Kosugi, K., Mizutani, T., & Mizuyama, T. (2009). Hydraulic properties of variously weathered granitic bedrock in headwater catchments. *Vadose Zone Journal*, 8(3), 557–573. <https://doi.org/10.2136/vzj2008.0142>
- Kirchner, J. W., Feng, X., & Neal, C. (2001). Catchment-scale advection and dispersion as a mechanism for fractal scaling in stream tracer concentrations. *Journal of Hydrology*, 254(1), 82–101. [https://doi.org/10.1016/S0022-1694\(01\)00487-5](https://doi.org/10.1016/S0022-1694(01)00487-5)
- Klaus, J., & McDonnell, J. (2013). Hydrograph separation using stable isotopes: Review and evaluation. *Journal of Hydrology*, 505, 47–64. <https://doi.org/10.1016/j.jhydrol.2013.09.006>
- Kollet, S. J., & Maxwell, R. M. (2008). Demonstrating fractal scaling of baseflow residence time distributions using a fully-coupled groundwater and land surface model. *Geophysical Research Letters*, 35(7), L07402. <https://doi.org/10.1029/2008GL033215>
- Leaf, A. T., & Fienen, M. N. (2022). Flopy: The Python interface for MODFLOW. *Groundwater*, 60(6), 710–712. <https://doi.org/10.1111/gwat.13259>
- Leray, S., Engdahl, N. B., Massoudieh, A., Bresciani, E., & McCallum, J. (2016). Residence time distributions for hydrologic systems: Mechanistic foundations and steady-state analytical solutions. *Journal of Hydrology*, 543, 67–87. <https://doi.org/10.1016/j.jhydrol.2016.01.068>
- Manning, A. H., & Caine, J. S. (2007). Groundwater noble gas, age, and temperature signatures in an alpine watershed: Valuable tools in conceptual model development. *Water Resources Research*, 43(4), W04404. <https://doi.org/10.1029/2006WR005349>
- Manning, A. H., Caine, J. S., Verplanck, P. L., Bove, D. J., & Kahn, K. G. (2009). US Geological Survey Research in Handcart Gulch, Colorado: An alpine watershed with natural acid-rock drainage. In *3rd Interagency Conference on Research in the Watersheds* (pp. 97–102).
- Maréchal, J., & Etcheverry, D. (2003). The use of ³H and ¹⁸O tracers to characterize water inflows in alpine tunnels. *Applied Geochemistry*, 18(3), 339–351. [https://doi.org/10.1016/S0883-2927\(02\)00101-4](https://doi.org/10.1016/S0883-2927(02)00101-4)
- Mari, L., Casagrandi, R., Bertuzzo, E., Rinaldo, A., & Gatto, M. (2014). Metapopulation persistence and species spread in river networks. *Ecology Letters*, 17(4), 426–434. <https://doi.org/10.1111/ele.12242>
- Markovich, K. H., Manning, A. H., Condon, L. E., & McIntosh, J. C. (2019). Mountain-block recharge: A review of current understanding. *Water Resources Research*, 55(11), 8278–8304. <https://doi.org/10.1029/2019WR025676>
- Maxwell, R. M., Condon, L. E., & Kollet, S. J. (2015). A high-resolution simulation of groundwater and surface water over most of the continental US with the integrated hydrologic model ParFlow v3. *Geoscientific Model Development*, 8(3), 923–937. <https://doi.org/10.5194/gmd-8-923-2015>
- McGuire, K. J., McDonnell, J. J., Weiler, M., Kendall, C., McGlynn, B. L., Welker, J. M., & Seibert, J. (2005). The role of topography on catchment-scale water residence time. *Water Resources Research*, 41(5), W05002. <https://doi.org/10.1029/2004WR003657>
- Meybeck, M., Green, P., & Vörösmarty, C. (2001). A new typology for mountains and other relief classes: An application to global continental water resources and population distribution. *Mountain Research and Development*, 21(1), 34–45. [https://doi.org/10.1659/0276-4741\(2001\)021\[0034:antfma\]2.0.co;2](https://doi.org/10.1659/0276-4741(2001)021[0034:antfma]2.0.co;2)
- Müller Schmied, H., Cáceres, D., Eisner, S., Flörke, M., Herbert, C., Niemann, C., et al. (2021). The global water resources and use model WaterGAP v2.2d: Model description and evaluation. *Geoscientific Model Development*, 14(2), 1037–1079. <https://doi.org/10.5194/gmd-14-1037-2021>
- Naz, B. S., Sharples, W., Ma, Y., Goergen, K., & Kollet, S. (2023). Continental-scale evaluation of a fully distributed coupled land surface and groundwater model, ParFlow-CLM (v3.6.0), over Europe. *Geoscientific Model Development*, 16(6), 1617–1639. <https://doi.org/10.5194/gmd-16-1617-2023>
- Niemi, A. J. (1977). Residence time distributions of variable flow processes. *The International Journal of Applied Radiation and Isotopes*, 28(10), 855–860. [https://doi.org/10.1016/0020-708X\(77\)90026-6](https://doi.org/10.1016/0020-708X(77)90026-6)
- Niswonger, R. G., Panday, S., & Ibaraki, M. (2011). MODFLOW-NWT, a Newton formulation for MODFLOW-2005 [Software]. *U.S. Geological Survey*, 6. Retrieved from <https://pubs.usgs.gov/tm/tm6a37/>
- Paul Köeniger, C. L., & Stichler, W. (2009). Spatial and temporal characterisation of stable isotopes in river water as indicators of groundwater contribution and confirmation of modelling results; a study of the Weser river, Germany. *Isotopes in Environmental and Health Studies*, 45(4), 289–302. <https://doi.org/10.1080/10256010903356953>
- Penna, D., van Meerveld, H., Zuecco, G., Dalla Fontana, G., & Borga, M. (2016). Hydrological response of an alpine catchment to rainfall and snowmelt events. *Journal of Hydrology*, 537, 382–397. <https://doi.org/10.1016/j.jhydrol.2016.03.040>
- Penna, D., Zuecco, G., Crema, S., Trevisani, S., Cavalli, M., Pianezzola, L., et al. (2017). Response time and water origin in a steep nested catchment in the Italian Dolomites. *Hydrological Processes*, 31(4), 768–782. <https://doi.org/10.1002/hyp.11050>
- Pollock, D. W. (2016). User guide for MODPATH Version 7—A particle-tracking model for MODFLOW [Software] (Technical Report). *U.S. Geological Survey*. <https://doi.org/10.3133/ofr20161086>
- Queloz, P., Bertuzzo, E., Carraro, L., Botter, G., Miglietta, F., Rao, P. S. C., & Rinaldo, A. (2015). Transport of fluorobenzoate tracers in a vegetated hydrologic control volume: 1. Experimental results. *Water Resources Research*, 51(4), 2773–2792. <https://doi.org/10.1002/2014WR016433>
- Queloz, P., Carraro, L., Benettin, P., Botter, G., Rinaldo, A., & Bertuzzo, E. (2015). Transport of fluorobenzoate tracers in a vegetated hydrologic control volume: 2. Theoretical inferences and modeling. *Water Resources Research*, 51(4), 2793–2806. <https://doi.org/10.1002/2014WR016508>
- Rapp, G. A., Condon, L. E., & Markovich, K. H. (2020). Sensitivity of simulated mountain block hydrology to subsurface conceptualization. *Water Resources Research*, 56(10), e2020WR027714. <https://doi.org/10.1029/2020WR027714>
- Reinecke, R., Foglia, L., Mehl, S., Trautmann, T., Cáceres, D., & Döll, P. (2019). Challenges in developing a global gradient-based groundwater model (G³M v1.0) for the integration into a global hydrological model. *Geoscientific Model Development*, 12(6), 2401–2418. <https://doi.org/10.5194/gmd-12-2401-2019>

- Rempe, D. M., & Dietrich, W. E. (2018). Direct observations of rock moisture, a hidden component of the hydrologic cycle. *Proceedings of the National Academy of Sciences*, 115(11), 2664–2669. <https://doi.org/10.1073/pnas.1800141115>
- Rinaldo, A., Gatto, M., & Rodriguez-Iturbe, I. (2018). River networks as ecological corridors: A coherent ecohydrological perspective. *Advances in Water Resources*, 112, 27–58. <https://doi.org/10.1016/j.advwatres.2017.10.005>
- Rinaldo, A., Gatto, M., & Rodriguez-Iturbe, I. (2020). *River networks as ecological corridors: Species, populations, pathogens*. Cambridge University Press. <https://doi.org/10.1017/9781108775014>
- Rodriguez, N. B., Pfister, L., Zehe, E., & Klaus, J. (2021). A comparison of catchment travel times and storage deduced from deuterium and tritium tracers using storage selection functions. *Hydrology and Earth System Sciences*, 25(1), 401–428. <https://doi.org/10.5194/hess-25-401-2021>
- Rodriguez-Iturbe, I., Muneepeerakul, R., Bertuzzo, E., Levin, S. A., & Rinaldo, A. (2009). River networks as ecological corridors: A complex systems perspective for integrating hydrologic, geomorphologic, and ecologic dynamics. *Water Resources Research*, 45(1), W01413. <https://doi.org/10.1029/2008WR007124>
- Rubin, Y. (2003). *Applied stochastic hydrogeology*. Oxford University Press.
- Schiavo, M. (2023). Entropy, fractality, and thermodynamics of groundwater pathways. *Journal of Hydrology*, 623, 129824. <https://doi.org/10.1016/j.jhydrol.2023.129824>
- Seeger, S., & Weiler, M. (2014). Reevaluation of transit time distributions, mean transit times and their relation to catchment topography. *Hydrology and Earth System Sciences*, 18(12), 4751–4771. <https://doi.org/10.5194/hess-18-4751-2014>
- Stadnyk, T., & Holmes, T. (2023). Large scale hydrologic and tracer aided modelling: A review. *Journal of Hydrology*, 618, 129177. <https://doi.org/10.1016/j.jhydrol.2023.129177>
- Staudinger, M., Stoelzle, M., Cochand, F., Seibert, J., Weiler, M., & Hunkeler, D. (2019). Your work is my boundary condition!: Challenges and approaches for a closer collaboration between hydrologists and hydrogeologists. *Journal of Hydrology*, 571, 235–243. <https://doi.org/10.1016/j.jhydrol.2019.01.058>
- Stewart, M. K., Morgenstern, U., & Cartwright, I. (2021). Comment on “A comparison of catchment travel times and storage deduced from deuterium and tritium tracers using StorAge Selection functions” by Rodriguez et al. (2021). *Hydrology and Earth System Sciences*, 25(12), 6333–6338. <https://doi.org/10.5194/hess-25-6333-2021>
- Tiedeman, C. R., Goode, D. J., & Hsieh, P. A. (1998). Characterizing a ground water basin in a New England mountain and valley terrain. *Groundwater*, 36(4), 611–620. <https://doi.org/10.1111/j.1745-6584.1998.tb02835.x>
- Tonkin, J. D., Altermatt, F., Finn, D. S., Heino, J., Olden, J. D., Pauls, S. U., & Lytle, D. A. (2018). The role of dispersal in river network metacommunities: Patterns, processes, and pathways. *Freshwater Biology*, 63(1), 141–163. <https://doi.org/10.1111/fwb.13037>
- Tóth, J. (1962). A theory of groundwater motion in small drainage basins in central Alberta, Canada. *Journal of Geophysical Research*, 67(11), 4375–4388. <https://doi.org/10.1029/JZ067i011p04375>
- Tóth, J. (1963). A theoretical analysis of groundwater flow in small drainage basins. *Journal of Geophysical Research*, 68(16), 4795–4812. <https://doi.org/10.1029/JZ068i016p04795>
- Tromp-van Meerveld, H. J., & McDonnell, J. J. (2006). Threshold relations in subsurface stormflow: 1. A 147-storm analysis of the Panola hillslope. *Water Resources Research*, 42(2), W02410. <https://doi.org/10.1029/2004WR003778>
- Ufficio Sistemi Informativi - Servizio autorizzazioni e valutazioni ambientali. (2013). LIDAR rilievo 2006/2007/2008 [Dataset]. *Dati Trentino*. Retrieved from <http://www.territorio.provincia.tn.it/portal/server.pt/community/lidar/847/lidar/23954>
- Visser, A., Thaw, M., Deinhart, A., Bibby, R., Safeeq, M., Conklin, M., et al. (2019). Cosmogenic isotopes unravel the hydrochronology and water storage dynamics of the Southern Sierra critical zone. *Water Resources Research*, 55(2), 1429–1450. <https://doi.org/10.1029/2018WR023665>
- Viviroli, D., Kumm, M., Meybeck, M., Kallio, M., & Wada, Y. (2020). Increasing dependence of lowland populations on mountain water resources. *Nature Sustainability*, 3(11), 917–928. <https://doi.org/10.1038/s41893-020-0559-9>
- Welch, L., & Allen, D. (2014). Hydraulic conductivity characteristics in mountains and implications for conceptualizing bedrock groundwater flow. *Hydrogeology Journal*, 22(5), 1003–1026. <https://doi.org/10.1007/s10040-014-1121-5>
- Winter, T. C., Rosenberry, D. O., & LaBaugh, J. W. (2003). Where does the ground water in small watersheds come from? *Groundwater*, 41(7), 989–1000. <https://doi.org/10.1111/j.1745-6584.2003.tb02440.x>
- Wolf, M. A., Jamison, L. R., Solomon, D. K., Strong, C., & Brooks, P. D. (2023). Multi-year controls on groundwater storage in seasonally snow-covered headwater catchments. *Water Resources Research*, 59(6), e2022WR033394. <https://doi.org/10.1029/2022WR033394>
- Wörman, A., Packman, A. I., Marklund, L., Harvey, J. W., & Stone, S. H. (2007). Fractal topography and subsurface water flows from fluvial bedforms to the continental shield. *Geophysical Research Letters*, 34(7). <https://doi.org/10.1029/2007GL029426>
- Yang, C., Tijerina-Kreuzer, D. T., Tran, H. V., Condon, L. E., & Maxwell, R. M. (2023). A high-resolution, 3D groundwater-surface water simulation of the contiguous US: Advances in the integrated ParFlow CONUS 2.0 modeling platform. *Journal of Hydrology*, 626, 130294. <https://doi.org/10.1016/j.jhydrol.2023.130294>
- Zehe, E., Lortz, R., Edery, Y., & Berkowitz, B. (2021). Preferential pathways for fluid and solutes in heterogeneous groundwater systems: Self-organization, entropy, work. *Hydrology and Earth System Sciences*, 25(10), 5337–5353. <https://doi.org/10.5194/hess-25-5337-2021>